Sonic hedgehog signaling directs patterned cell remodeling during cranial neural tube closure

Eric R. Brooks[1], Mohammed T. Islam[1], Kathryn V. Anderson[2], and Jennifer A. Zallen[1,3]

[1]Howard Hughes Medical Institute and Developmental Biology Program, Sloan Kettering Institute, New York, NY, USA

[2]Developmental Biology Program, Sloan Kettering Institute, New York, NY, USA

[3]**For correspondence:** zallenj@mskcc.org

Competing interests: The authors declare that no competing interests exist.

Abstract

Neural tube closure defects are a major cause of infant mortality, with exencephaly accounting for nearly one-third of cases. However, the mechanisms of cranial neural tube closure are not well understood. Here we show that this process involves a tissue-wide pattern of apical constriction controlled by Sonic hedgehog (Shh) signaling. Midline cells in the mouse midbrain neuroepithelium are short with large apical surfaces, whereas lateral cells are taller and undergo synchronous apical constriction, driving neural fold elevation. Embryos lacking the Shh effector Gli2 fail to produce appropriate midline cell architecture, whereas embryos with expanded Shh signaling, including the IFT-A complex mutants *Ift122* and *Ttc21b* and embryos expressing activated Smoothened, display apical constriction defects in lateral cells. Disruption of lateral, but not midline, cell remodeling results in exencephaly. These results reveal a morphogenetic program of patterned apical constriction governed by Shh signaling that generates structural changes in the developing mammalian brain.

Introduction

Neural tube closure defects are among the most common structural birth defects, occurring in 1 in 1,000 pregnancies worldwide (Wallingford et al., 2013; Zaganjor et al., 2016). During development, neuroepithelial cells undergo extensive remodeling to transform a flat sheet into a fully closed tube that gives rise to the brain and spinal cord of the animal. Distinct genetic circuits are required for neural tube closure in different regions along the head-to-tail axis, translating positional information into location-appropriate cell behaviors (Wilde et al., 2014; Aw and Devenport, 2017; Nikolopoulou et al., 2017; Juriloff and Harris, 2018). Although many studies have focused on mechanisms of neural tube closure in the spinal cord, one-third of human neural tube defects arise from a failure of closure in the cranial region, resulting in exencephaly—an inoperable and terminally lethal birth defect (Zaganjor et al., 2016). More than a hundred genes are specifically required for closure of the mouse cranial neural plate, suggesting that unique mechanisms promote neural tube closure in the cranial region (Harris and Juriloff, 2007; Harris and Juriloff, 2010; Wilde et al., 2014). Despite the clinical importance of this disease, the cellular mechanisms that produce cranial neural tube structure, and how these cell behaviors are coordinated across thousands of cells to close the massive cranial region, remain opaque.

Tissue-scale structural changes during cranial neural closure require the precise spatial regulation of cell behaviors along the anterior-posterior and mediolateral axes. However, how cell behaviors are dynamically patterned along these axes is only beginning to be understood. The neural plate is significantly wider in the cranial region compared with the spinal cord, suggesting that distinct strategies may be required for closure of the developing brain. In addition, positionally regulated signals produce distinct cell fates along the mediolateral axis of the neural tube. Neuronal identities at different mediolateral positions are regulated by the secreted Shh, Wnt, and BMP proteins, with high levels of Shh producing ventral cell fates, moderate levels of Shh producing intermediate cell fates, and high levels of Wnt and BMP producing dorsal cell fates (McMahon et al., 2003; Dessaud et al., 2008; Sagner and Briscoe, 2019). In the posterior spinal cord, spatially restricted Shh and BMP signaling are required for local tissue bending, suggesting that these signals can influence tissue structure as well as cell identity (Ybot-Gonzalez et al., 2002; Ybot-Gonzalez et al., 2007). However, the cell behaviors that drive cranial neural tube closure and the positional signals that determine where and when these behaviors occur in the tissue are unknown.

Midline cells are essential drivers of neural tube closure in the spinal cord across the chordate lineage, undergoing cell-shape changes (Burnside and Jacobson, 1968; Smith et al., 1994; Haigo et al., 2003; Lee et al., 2007; Nishimura and Takeichi, 2008; Nishimura et al., 2012; McShane et al., 2015) and planar rearrangements (Davidson and Keller, 1999; Wallingford and Harland, 2002; Williams et al., 2014; Sutherland et al., 2020) that narrow and bend the neural plate. At later stages of closure, cells at the borders of the neural plate form dynamic protrusions and adhesions that join the left and right sides of the neural plate to produce a closed tube (Pyrgaki et al., 2010; Massarwa et al., 2014; Hashimoto et al., 2015; Ray and Niswander, 2016a; Ray and Niswander, 2016b; Molè et al., 2020). However, it is not known if localized forces at the midline and borders of the neural plate are sufficient for closure of the significantly larger cranial region, or if distinct cell populations and behaviors contribute to cranial neural structure.

Apical constriction is a highly conserved process that transforms columnar epithelial cells into wedge shapes through actomyosin-dependent contraction of the apical cell surface and drives structural changes such as cell ingression, tissue bending, and tissue invagination (Martin and Goldstein, 2014). In the amphibian neural plate, apical constriction is required to form the

median and dorsolateral hinge points, two localized tissue bending events that are a prerequisite for closure (Burnside and Jacobson, 1968; Burnside, 1973; Haigo et al., 2003; Lee et al., 2007; Itoh et al., 2014; Ossipova et al., 2014). However, it is not known if apical constriction contributes to closure in the tightly packed, pseudostratified neuroepithelium of the mammalian neural plate. In the mouse spinal cord, neural tube closure is independent of actomyosin activity, suggesting that apical constriction is not required for this process (Ybot-Gonzalez and Copp, 1999; Escuin et al., 2015). Instead, bending of the developing spinal cord is proposed to occur through alternative mechanisms such as tissue buckling or cell-cycle-dependent changes in nuclear position (McShane et al., 2015; Nikolopoulou et al., 2017). By contrast, regulators of actin and myosin are required for closure of the cranial neural plate, although the cell behaviors that are controlled by this contractile machinery are unclear (Morriss-Kay and Tuckett, 1985; Hildebrand and Soriano, 1999; Brouns et al., 2000; McGreevy et al., 2015). Loss of the actomyosin regulator Shroom3 leads to an increase in apical cell surface area in the cranial neuroepithelium, consistent with a defect in apical constriction (McGreevy et al., 2015). However, mammalian cranial neuroepithelial cells also undergo significant elongation along the apicobasal axis that can decrease the apical surface of cells independently of apical constriction (Jacobson and Tam, 1982), and several mutants defective for apicobasal elongation, including *Pten, Cfl1*, and *Nuak1/2* mutants, also show an increase in apical cell area (Ohmura et al., 2012; Grego-Bessa et al., 2015; Grego-Bessa et al., 2016). Disambiguating the contributions of apical constriction and apicobasal elongation to cranial closure is challenging, in part due to the difficulty in visualizing individual cell shapes in this densely packed tissue. Therefore, the cell behaviors that promote cranial neural closure, and the critical force-generating cell populations that drive these dynamic changes, are unknown.

Using high-resolution imaging of cell behavior in the mouse cranial neural plate, we demonstrate a tissue-wide pattern of apical constriction during neural tube closure in the developing midbrain. In contrast to the spinal cord, elevation of the cranial neural folds is driven by the synchronous, sustained apical constriction of a large population of lateral cells, whereas midline cells remain flat and apically expanded. The loss of Gli2, a transcriptional effector of Shh signaling, disrupts cell architecture at the midline, whereas loss of the IFT-A complex components Ift122 or Ttc21b disrupt apical constriction and actomyosin organization in lateral cells, resulting in a failure of cranial neural tube closure. These apical remodeling defects are recapitulated by activation of the Shh response throughout the midbrain, indicating that they are due to deregulated Shh signaling. Together, these results demonstrate that lateral cells drive

cranial neural tube closure through large-scale, coordinated apical constriction behaviors that are spatially regulated by patterned Shh activity.

Results

Neuroepithelial cells display patterned apical constriction during cranial closure

A critical step in the closure of the mouse midbrain is the transformation of the neural plate from convex to concave (Figure 1A-C) (Nikolopoulou et al., 2017; Vijayraghavan and Davidson, 2017; Juriloff and Harris, 2018). Prior to closure, the cranial neural plate has an open, rams-horn shape (Figure 1C). The neuroepithelial sheet is convex on either side of the midline, with the outer edges of the neural plate tucked under the lateral regions. This curvature reverses during neural fold elevation, when both sides of the neural plate rise up and straighten to produce a concave, V-shaped structure (Figure 1C). The borders of the neural plate subsequently bend inward, appose, and fuse at the dorsal midline to produce a closed tube. To investigate the cell behaviors that drive these structural changes, we used confocal imaging and semi-automated image segmentation (Mashburn et al., 2012; Farrell et al., 2017) to analyze cell behavior at single-cell resolution. The apical profiles of midbrain neuroepithelial cells were relatively homogeneous in area prior to elevation (0 somites, E7.75) (Figure 1D and E). However, a strong pattern emerged during elevation (6 somites, E8.5). Lateral cells on either side of the midline displayed a more than 50% decrease in apical area between 0 and 9 somites (Figure 1F-H, Supplementary File 1). By contrast, the average apical surface area of midline cells did not change significantly during elevation (Figure 2A-C). Additionally, lateral cells became progressively mediolaterally oriented during the same period, whereas midline cell orientation was unchanged (Figure 2-figure supplement 1). These results indicate that lateral cells, but not midline cells, undergo apical remodeling during cranial neural fold elevation.

The finding that midline cells in the midbrain do not remodel during neural fold elevation differs from neural tube closure mechanisms in the spinal cord, in which wedge-shaped midline cells drive tissue bending (McShane et al., 2015; Schoenwolf and Franks, 1984; Smith et al., 1994; Smith and Schoenwolf, 1988), and raises the possibility that lateral cells may be key drivers of elevation. To determine if the apical remodeling of lateral cells is due to apicobasal elongation, we analyzed cell height in the cranial neural plate at different stages of elevation. Cell height in

the lateral and midline regions did not change significantly during early elevation (0-7 somites) (Figure 3C and D), even though the average apical area of lateral cells decreased by more than 30% during this period (Figure 1G). By contrast, lateral and midline cells elongated more than 60% along the apical-basal axis after the 7-somite stage, such that lateral cells were consistently taller than midline cells throughout elevation (Figure 3C-E). Thus, cell remodeling in the elevating midbrain occurs in two phases, with an early phase involving apical remodeling in the absence of changes in cell height, and a later phase involving apicobasal elongation (Figure 3J). These results indicate that apicobasal elongation in the neuroepithelium occurs at late stages of elevation, but cannot explain the dramatic structural changes that occur during early elevation.

We next investigated whether apical constriction contributes to early structural changes in the midbrain neuroepithelium. Consistent with this possibility, the conversion of the midbrain neural plate from convex to concave is accompanied by a decrease in the apical span of the tissue without a significant change in the basal span (Figure 3A and B, Figure 3–figure supplement 1A and B). However, apical constriction has not been directly observed in the pseudostratified mammalian neural plate, where the crowded packing of cells has been proposed to hinder this process (Nikolopoulou et al., 2017). To determine if lateral cells undergo apical constriction, we visualized cell morphology in the midbrain neuroepithelium of embryos expressing membrane-GFP in a mosaic pattern, using the inefficient EIIA-Cre recombinase to label individual cells (Figure 3F) (Lakso et al., 1996; Muzumdar et al., 2007). Using this approach, we identified five classes of lateral cells (Figure 3G). More than half of lateral cells (51±6%) had a highly constricted apical neck, a hallmark of apical constriction. An additional 13±2% displayed properties consistent with apical constriction, but with a shorter neck domain, suggesting that apical area changes can occur even in the absence of a basal shift in cell volume. The remaining one-third of lateral cells were apically expanded, spindle-shaped, or columnar. Because few midline cells were labeled by this method, we used manual segmentation to investigate cell shape at the midline using antibodies to β-catenin (Figure 3H). In contrast to lateral cells, midline cells tended to be columnar (45±5%) or apically expanded (30%), with relatively few midline cells showing apically constricted morphologies (17±3%) (Figure 3I, Figure 3–figure supplement 2A and B). These results directly demonstrate the presence of apical constriction in the lateral neural plate and reveal a striking regionalization of cell-shape changes along the mediolateral axis.

205 **Apical remodeling and cranial neural closure require IFT-A proteins**
206
207 To identify the mechanisms that regulate the distinct behaviors of lateral and midline cells, we
208 sought to identify mutants that disrupt this pattern. In a genetic screen for mouse mutants with
209 embryonic defects (García-García et al., 2005), we identified two mutants with severe defects in
210 cranial neural closure (Figure 4A-C). The mutations in these strains mapped to premature stop
211 codons in *Ift122* and *Ttc21b (Ift139)*, which encode components of the conserved intraflagellar
212 transport A (IFT-A) complex (Figure 4–figure supplement 1A and B). The IFT-A complex directs
213 the trafficking of structural and signaling proteins in cilia, microtubule-based cellular organelles
214 that modulate Shh signaling (Wong and Reiter, 2008; Bangs and Anderson, 2017). Consistent
215 with these functions, mutant embryos from both strains exhibited a reduction in the number of
216 cilia (Figure 4–figure supplement 1C-E). Mutations in IFT-A complex components have been
217 shown to cause exencephaly, but how these proteins influence cranial neural closure is not
218 known (Tran et al., 2008; Cortellino et al., 2009; Murdoch and Copp, 2010; Qin et al., 2011;
219 Bangs and Anderson, 2017). In contrast to littermate controls, which completed neural fold
220 elevation, apposition, and fusion in 24 hours, *Ift122* and *Ttc21b* mutants failed to generate V-
221 shaped neural folds in the midbrain, forebrain, and anterior hindbrain regions of 7-somite
222 embryos (Figure 4D-F, Figure 4–figure supplements 2 and 3). These defects did not recover
223 and the cranial neural folds of mutant embryos remained unelevated at all stages analyzed,
224 leading to highly penetrant exencephaly at E10.5 (Figure 4A-C). Thus, the cranial closure
225 defects in *Ift122* and *Ttc21b* mutants arise from an early failure in cranial neural fold elevation.
226
227 To determine the cellular basis of these exencephaly defects, we analyzed cell shape in *Ift122*
228 and *Ttc21b* mutants. Mutant embryos displayed a striking expansion of the apical cell surface in
229 the lateral midbrain (Figure 4G-I). Lateral cells in *Ift122* and *Ttc21b* mutants displayed a 55%
230 and 93% increase in average apical cell area, respectively, compared with littermate controls
231 (Figure 4J-M), as well as altered cell orientation (Figure 4-figure supplement 4). These defects
232 did not result from reduced cell proliferation, as mutant embryos had a normal frequency and
233 distribution of mitotic cells along the mediolateral axis, and normal cell density in the underlying
234 mesenchyme (Figure 4-figure supplements 5 and 6). These results indicate that *Ift122* and
235 *Ttc21b* are required for cell-shape changes in the lateral midbrain neuroepithelium.
236
237
238

IFT-A proteins pattern cell shape and actomyosin contractility

To determine if the global pattern of cell remodeling is affected in IFT-A mutants, we examined cell-shape changes throughout the entire mediolateral axis of the midbrain in *Ift122* and *Ttc21b* mutants. In wild-type littermate controls, apically expanded cells were present at the midline and at the outer margins of the tissue. These domains were separated by a broad domain of apically constricted cells spanning 30-40 cell diameters along the mediolateral axis and more than 60 cells along the anterior-posterior axis, encompassing a region of more than 2,000 lateral cells on either side of the midline (Figure 5A and F-H). The difference between midline and lateral populations was eliminated in *Ift122* and *Ttc21b* mutants (Figure 5B-E). In mutant embryos, lateral cells were apically expanded and midline cells were apically constricted compared with controls, whereas cell shape at the outer margins of the neural plate was independent of IFT-A activity (Figure 5F-H). Moreover, the difference in height between wild-type midline and lateral cells was abolished in *Ift122* and *Ttc21b* mutants (Figure 5I and J, Figure 5–figure supplement 1A and B). These cell remodeling defects were associated with a failure to fully convert the cranial region from convex to concave in *Ift122* and *Ttc21b* mutants (Figure 5–figure supplement 1C-F). These results demonstrate that Ift122 and Ttc21b are required for patterned apical remodeling in the midbrain neuroepithelium. In their absence, midline and lateral cells adopt a uniform cell morphology.

A hallmark of apical constriction is the requirement for apically localized actomyosin contractility (Martin and Goldstein, 2014). To determine if this is the mechanism by which Ift122 and Ttc21b promote apical remodeling in lateral cells, we analyzed the localization of F-actin and the phosphorylated (active) form of myosin II in *Ift122* and *Ttc21b* mutants. Wild-type cranial neuroepithelial cells display a strong accumulation of F-actin and phosphomyosin at the apical cell cortex, which is often assembled into mediolaterally oriented actomyosin cables in the chick and mouse neural plate (Nishimura et al., 2012; McGreevy et al., 2015). In line with these observations, we observed frequent supracellular cables in the elevating cranial neural plate. Cables were present at a range of orientations, with a strong mediolateral bias (Figure 6A, B, E, and F). By contrast, fewer actomyosin cables were present in *Ift122* and *Ttc21b* mutants, and the cables that did form were not consistently oriented with respect to the mediolateral axis (Figure 6A-F). The ratio of phosphomyosin to F-actin at adherens junctions was also decreased in *Ttc21b* mutants (Figure 6G and H), consistent with the stronger apical constriction defects in

this mutant. These results demonstrate that Ift122 and Ttc21b are required for apical actomyosin organization in the midbrain neuroepithelium.

Shh signaling organizes patterned apical remodeling

Cilia are signaling organelles that are critical for Shh signaling and cell fate. Our finding that cilia proteins are also required for cell remodeling suggests that fate and morphology may be directly linked. In the spinal cord, the loss of IFT-A complex function typically results in ligand-independent activation of Shh signaling and an expansion of Shh-dependent ventral cell fates (Tran et al., 2008; Cortellino et al., 2009; Qin et al., 2011; Bangs and Anderson, 2017), although strong disruption of IFT-A function can result in a loss of Shh-dependent cell fates (Liem et al., 2012). To test whether Ift122 and Ttc21b pattern cell fate during cranial neural fold elevation, we analyzed the expression of Nkx6.1, a target of Shh signaling. In wild-type embryos, Nkx6.1 levels were highest at the midline during midbrain neural fold elevation and decreased with increasing distance from the midline (Figure 7A and B), consistent with results at later stages (Qiu et al., 1998; Tran et al., 2008; Qin et al., 2011; Tang et al., 2013). In addition, Nkx6.1 was expressed at lower levels in the anterior hindbrain, revealing differential regulation along the anterior-posterior axis (Figure 7A). In *Ift122* and *Ttc21b* mutants, the mediolateral pattern of Nkx6.1 expression was abolished, and Nkx6.1 was expressed at equivalent, intermediate levels in midline and lateral cells (Figure 7A-C). In addition, the mediolateral extent of the Nkx6.1 domain was expanded, reaching all the way to the neural plate borders in *Ift122* and *Ttc21b* mutants. By contrast, the anterior-posterior pattern of Nkx6.1 expression was unaffected, indicating that this axis of Shh regulation is independent of IFT-A activity. These results raise the possibility that deregulated Shh signaling could underlie the cranial closure defects in *Ift122* and *Ttc21b* mutants.

To investigate the role of Shh signaling in midbrain cell remodeling, we examined cell morphology in mutants lacking the Shh effector Gli2, which is required to generate ventral Shh-dependent cell types (Mo et al., 1997; Matise et al., 1998; Bai et al., 2002; Wong and Reiter 2008; Bangs and Anderson, 2017). Because Shh signaling is normally highest at the midline, we asked if the unique architecture of midline cells requires Gli2 function. Consistent with the effects of Gli2 at later stages, *Gli2* mutants failed to establish ventral cell fates in the elevating midbrain, including FoxA2 expression in the floor plate, indicating that Gli2 is required for

midline cell identity (Figure 8-figure supplement 1). Midline cells in *Gli2* mutants had a significant decrease in apical area compared with wild type (Figure 8D-F). In addition, midline cells in *Gli2* mutants were significantly taller than in wild-type controls (Figure 8G and H). By contrast, lateral cell morphology was unaffected in *Gli2* mutants (Figure 8A-C, G, and H), and no defects in cell orientation were observed in either region (Figure 8-figure supplement 2). These data demonstrate that Gli2 activity is necessary for the short, apically expanded architecture of midline cells but not for apical constriction in lateral cells. Despite these severe midline defects, *Gli2* mutants complete closure normally in both cranial and spinal regions (Mo et al., 1997; Matise et al., 1998; Bai et al., 2002), indicating that the specialized architecture of midline cells is dispensable for cranial neural tube closure.

Because cranial neural tube closure occurs normally in the absence of proper midline morphology, we hypothesized that a failure of apical constriction in lateral cells could be responsible for the cranial closure defects in *Ift122* and *Ttc21b* mutants. In addition, the expanded Nkx6.1 expression in *Ift122* and *Ttc21b* mutants raises the possibility that increased Shh signaling in lateral cells could underlie the defects in apical constriction. To test these hypotheses, we investigated whether spatially restricted Shh signaling is required for apical constriction and cranial neural closure. We ectopically activated the Shh signaling response throughout the midbrain by expressing a constitutively active variant of the Shh receptor Smoothened (SmoM2) (Jeong et al., 2004) using Wnt1-Cre2 (Lewis et al., 2013). SmoM2-expressing embryos have expanded Nkx6.1 expression throughout the midbrain, consistent with uniform activation of the Shh response (Figure 9C and D). SmoM2 expression did not affect cell proliferation or cell orientation (Figure 9–figure supplements 1 and 2). However, SmoM2 expression resulted in a 50% increase in apical area in lateral cells (Figure 9G-I), similar to the defects in *Ift122* mutants, but less severe than the defects in *Ttc21b* mutants. The effects of SmoM2 were localized, as cells that did not express Wnt1-Cre2 apically constricted normally, suggesting that activated SmoM2 acts cell autonomously to regulate cell shape (Figure 9E and F). SmoM2-expressing embryos did not display morphological defects at the midline, perhaps because Smoothened activation did not further enhance the already high Shh response in this region (Figure 9G, J and K). Notably, SmoM2-expressing embryos exhibited 100% penetrant exencephaly (12/12 SmoM2-expressing embryos compared with 0/13 littermate controls) (Figure 9A and B). These results demonstrate that disruption of apical constriction in lateral cells alone—in the absence of structural changes at the midline—is sufficient to prevent cranial neural closure. Thus, patterned Shh signaling in the midbrain neuroepithelium is required for

spatially regulated apical remodeling events that drive cranial neural closure, and dysregulation of Shh activity leads to altered cell remodeling and exencephaly (Figure 9L and M).

Discussion

Neural tube closure defects are among the most common human birth defects, with one-third of cases arising from defects in closure of the cranial region (Zaganjor et al., 2016). However, the mechanisms that convert the large cranial neural plate region from convex to concave during neural tube closure have long been obscure. Here we show that elevation is driven by a tissue-scale pattern of apical cell remodeling in the mouse midbrain in which thousands of lateral cells undergo synchronous, sustained apical constriction, whereas midline cells remain apically expanded. Spatiotemporally regulated cell remodeling in this system requires patterned Shh signaling. Loss of the Shh effector Gli2 results in a failure to establish the short and flat morphology of cells at the midline, but does not prevent neural tube closure. By contrast, expansion of Shh signaling into the lateral neural plate, either in IFT-A mutants that impair cilia-dependent Shh regulation or in embryos that express activated Smoothened throughout the midbrain neuroepithelium, leads to a disruption of apical constriction in lateral cells and results in highly penetrant exencephaly. These results reveal a program of positionally encoded cell behavior that is essential for neural tube closure in the developing midbrain and identify Shh as a critical regulator of coordinated cell remodeling in the mammalian cranial neural plate.

Lateral cells that undergo apical constriction and midline cells that do not are distinguished by their distance from the source of the Shh signal, as the Shh response is normally high at the midline and diminished laterally (Qiu et al., 1998; Sagner and Briscoe, 2019; Tang et al., 2013). The morphological changes in embryos with a reduced or expanded response to Shh signaling are consistent with a model in which high levels of Shh signaling induce short, apically expanded cells, whereas low levels of Shh signaling are associated with tall, apically constricted cells. *Gli2* mutants that disrupt specific aspects of Shh signaling are defective for cell-shape changes in midline cells where Shh signaling is normally high (Figure 9L and M). By contrast, in SmoM2-expressing embryos that have aberrantly high Shh signaling throughout the midbrain, midline morphology is normal, but lateral cells fail to apically constrict. IFT-A mutants that have a uniform, intermediate level of Shh signaling throughout the midbrain display equivalent cell morphologies in both regions. These results are consistent with a model in which different levels of Shh signaling induce different cell shapes in the midbrain neuroepithelium, with high levels of

Shh signaling inhibiting apical remodeling and apicobasal cell elongation at the midline, and low levels of Shh signaling allowing apical constriction in lateral cells. Thus, Shh not only determines the pattern of cell fates in the tissue, but is also essential for the organized cell behaviors that establish tissue structure. These dual functions of Shh provide a single source of positional information that regulates both cell identity and cell morphology, linking tissue pattern to tissue structure.

Apical constriction is a potent and conserved mechanism for generating changes in cell shape (Martin and Goldstein, 2014). During morphogenesis, apical constriction in a narrow or spatially delimited domain promotes localized tissue bending or invagination, as in *Drosophila* ventral furrow formation (Ko and Martin, 2020)*, C. elegans* gastrulation (Lee and Goldstein, 2003; Lee et al., 2006), *Xenopus* blastopore invagination (Keller, 1981; Lee and Harland, 2007; Lee and Harland, 2010), and hinge point formation in the vertebrate spinal cord (Haigo et al., 2003; Lee et al., 2007; Vijayraghavan and Davidson, 2017). By contrast, we show that widespread apical constriction events are coordinated across thousands of cells in the developing midbrain, resulting in a large-scale change in the curvature of the elevating neural plate. Coordinated apical constriction in large cell populations has been observed in tissues that undergo a dramatic change or even an inversion of tissue curvature, such as in the mouse lens placode, which transitions from flat to spherical (Plageman et al., 2010), and in colonies of adherent unicellular choanoflagellates undergoing light-dependent curvature inversion (Brunet et al., 2019). Thus, coordinated constriction among hundreds to thousands of cells may represent an evolutionarily conserved mechanism for collectively promoting large-scale curvature changes in multicellular tissues.

The cell-shape defects caused by an expanded Shh response in IFT-A mutants suggest a unifying hypothesis for the cranial closure defects in mutants with deregulated Shh signaling (Murdoch and Copp, 2010), including mutants that affect cilia structure (Liem et al., 2012), transducers of the Shh signal such as Gli3 and Sufu (Hui and Joyner, 1993; Svärd et al., 2006), and negative regulators of the Shh response (Ikeda et al., 2001; Cameron et al., 2009; Norman et al., 2009; Patterson et al., 2009). Expanded Shh signaling could inhibit apical constriction through a canonical signaling pathway involving Gli2- and Gli3-mediated transcriptional changes (Dessaud et al., 2008; Kicheva and Briscoe, 2015; Bangs and Anderson, 2017; Sagner and Briscoe, 2019), possibly involving repression of the BMP inhibitor Noggin, which promotes tissue bending in the spinal cord (Ybot-Gonzalez et al., 2002; Ybot-Gonzalez et al., 2007; Eom

et al., 2011). Consistent with this possibility, the loss of Noggin has been shown to cause exencephaly (Stottmann et al., 2006). Alternatively, Shh could regulate cell shape through a noncanonical signaling pathway (Robbins et al., 2012; de la Roche et al., 2013; Zuñiga and Stoeckli, 2017). Elucidation of these effector pathways will reveal how cell morphology and cell fate are coordinately regulated in response to the Shh signal.

Shh signaling has long been recognized to play an important role in controlling positional cell fates in many developing organs, including the limb, the gut, and the spinal cord (Jessell, 2000; Villavicencio et al., 2000; McMahon et al., 2003; McGlinn and Tabin, 2006; Tickle and Towers, 2017; Sagner and Briscoe, 2019). Although the effects of Shh on cell behavior have received comparatively less attention, Shh has been shown to influence axon guidance (Zuñiga and Stoeckli, 2017), cell migration (Gordon et al., 2018), mesenchymal cell clustering (Rao-Bhatia et al., 2020), and epithelial remodeling in mice, chicks, frogs, and flies (Corrigall et al., 2007; Escudero et al., 2007; Nasr et al., 2019; Arraf et al., 2020). Depending on the context, proteins in the Shh family can have contrasting effects on epithelial cell behavior, promoting apical constriction in the *Drosophila* eye (Corrigall et al., 2007; Escudero et al., 2007), generating short and flat cells in the neural tube (Fournier-Thibault et al., 2009 and this work), and inducing tall, pseudostratified cells in the chick coelomic cavity (Arraf et al., 2020). An understanding of the mechanisms by which Shh signaling directs cell morphology will provide insight into how this conserved, positionally encoded molecular mechanism coordinates cell fate with three-dimensional tissue structure.

Materials and Methods

Key Resources Table				
Reagent type (species) or resource	**Designation**	**Source or reference**	**Identifiers**	**Additional information**
Genetic reagent (*Mus musculus*)	FVB/NJ	Jackson Laboratory	stock no. 001800 RRID:IMSR_JAX:001800	
Genetic reagent (*Mus musculus*)	*Ift122*^{TR2}	This study		FVB/N background
Genetic reagent (*Mus musculus*)	*Ttc21b*^{TF2}	This study		FVB/N background
Genetic reagent (*Mus musculus*)	SmoM2	Jackson Laboratory (Jeong et al., 2004)	*Gt(ROSA)26Sor*$^{tm1(Smo/EYFP)Amc}$/J stock no. 005130 MGI:3576373 RRID:IMSR_JAX:005130	C57BL/6J background
Genetic reagent (*Mus musculus*)	*Wnt1-Cre2*	Jackson Laboratory (Lewis et al., 2013)	*E2f1*$^{Tg(Wnt1-cre)2Sor}$/J stock no. 022137 MGI:5485027 RRID:IMSR_JAX:022137	FVB/N background
Genetic reagent (*Mus musculus*)	EIIA-Cre	Jackson Laboratory (Lasko et al., 1996)	Tg(EIIa-cre)C5379Lmgd/J stock no. 003314 MGI:2137691 RRID:IMSR_JAX:003314	FVB/N background

Genetic reagent (*Mus musculus*)	*mT/mG*	Jackson Laboratory (Muzumdar et al., 2007)	*Gt(ROSA)26Sor*$^{tm4(ACTB-tdTomato,-EGFP)Luo}$/J stock no. 007676 MGI:3716464 RRID:IMSR_JAX:007676	FVB/N background
Genetic reagent (*Mus musculus*)	*Gli2*^{lzki}	Jackson Laboratory (Bai et al., 2001)	*Gli2*$^{tm2.1Alj}$/J stock no. 007922 MGI:3815004 RRID:IMSR_JAX:007922	SWR/J background
Antibody	anti-ZO-1 (rat monoclonal)	Develop-mental Studies Hybridoma Bank (DSHB)	R26.4C RRID:AB_2205518	(1:100)
Antibody	anti-phospho-Histone H3 (rabbit polyclonal)	Upstate	06-570 RRID:AB_310177	(1:1,000)
Antibody	anti-Arl13b (rabbit polyclonal)	Caspary et al., 2007		(1:1,000)
Antibody	anti-β-catenin (mouse monoclonal)	BD	610153 RRID:AB_397554	(1:300)
Antibody	anti-laminin (rabbit polyclonal)	Sigma	L9393 RRID:AB_477163	(1:1,000)
Antibody	anti-N-cadherin (rabbit monoclonal)	Cell Signaling Technology	D4R1H RRID:AB_2687616	(1:500)

Antibody	anti-GFP (chicken polyclonal)	abcam	ab13970 RRID:AB_300798	(1:1,000)
Antibody	anti-Nkx6.1 (mouse monoclonal)	DSHB	F55A10 RRID:AB_532378	(1:50)
Antibody	anti-diphospho myosin regulatory light chain (rabbit polyclonal)	Cell Signaling Technology	3674 RRID:AB_2147464	(1:100)
Antibody	anti-FoxA2 (rabbit monoclonal)	abcam	ab108422 RRID:AB_11157157	(1:1,000)
Sequence-based reagent	Ift122(TR2)_F	This study	PCR primer	CTGGTTGT AATCTGAC TCGTTGA After amplification with below reverse primer, product is digested with HpyCH4III, resulting in a 133 bp WT band and a 118 bp mutant band.
Sequence-based reagent	Ift122(TR2)_ R	This study	PCR primer	ACTCCCAA GCAAGCGA ACT
Sequence-based reagent	Ttc21b(TF2)_ F	This study	PCR primer	AGAATGAT GTGCAACC TTGTTGA

				After amplification with below reverse primer, product is digested with NmuCI, resulting in a 224 bp WT band and a 168 bp mutant band.
Sequence-based reagent	Ttc21b(TF2)_R	This study	PCR primer	TTATCTGG CTCACGGT CTCC
Software, algorithm	SeedWater Segmenter	Mashburn et al., 2012		
Software, algorithm	SEGGA	Farrell et al., 2017		
Software, algorithm	FIJI/ImageJ	Schindelin et al., 2012 Schneider et al., 2012	RRID:SCR_002285	
Software, algorithm	MorphoLibJ (FIJI plugin)	Legland et al., 2016		
Software, algorithm	ITK-SNAP	Yushkevich et al., 2006	RRID:SCR_002010	
Software, algorithm	R	R Core Team, 2020	RRID:SCR_001905	

Software, algorithm	Circular plugin (for R)	Agonstinelli and Lund, 2017		
Software, algorithm	Prism	Graphpad	RRID:SCR_002798	
Software, algorithm	Zen	Zeiss	RRID:SCR_018163	
Software, algorithm	LAS X	Leica	RRID:SCR_013673	
Software, algorithm	EOS Utility	Canon		
Software, algorithm	Illustrator	Adobe	RRID:SCR_010279	

Mouse strains

The *Ift122*^{TR2} and *Ttc21b*^{TF2} alleles were identified in an ongoing forward genetic screen (García-García et al., 2005). The *Ift122*^{TR2} mutation was mapped to a single C to A mutation at position 115,899,529 on chromosome 6, resulting in a premature stop codon that is predicted to truncate the protein at amino acid 575 (out of 1,138). The *Ttc21b*^{TF2} allele was mapped to a single C to A mutation at position 66,242,780 on chromosome 2, resulting in a premature stop codon that is predicted to truncate the protein at amino acid position 187 (out of 1,315). Both alleles created a new restriction site. The presence of the *Ift122*^{TR2} allele was genotyped by PCR amplification with the primers TR2F 5' CTGGTTGTAATCTGACTCGTTGA 3' and TR2R 5' ACTCCCAAGCAAGCGAACT 3' followed by restriction digest with HpyCH4III (New England Biolabs). The presence of the *Ttc21b*^{TF2} allele was genotyped by PCR amplification with the primers TF2F 5' AGAATGATGTGCAACCTTGTTGA 3' and TF2R 5' TTATCTGGCTCACGGTCTCC 3' followed by restriction digest with NmuCI (ThermoFisher Scientific). The following previously described mouse strains were used in this study: Wnt1-Cre2 [Tg(Wnt1-cre)2Sor] (Lewis et al., 2013), EIIA-Cre [Tg(EIIa-Cre)C5379Lmgd/J] (Lakso et al., 1996), mT/mG [Gt(ROSA)26Sortm4(ACTB-tdTomato,-EGFP)Luo/J] (Muzumdar et al.,

2007), SmoM2 [Gt(ROSA)26Sortm1(Smo/YFP)Amc/J] (Jeong et al., 2004), and Gli2 [Gli2$^{tm2.1Alj}$/J] (Bai et al., 2001). All lines were maintained in an FVB/N background except SmoM2, which was maintained in a C57BL/6J background, and *Gli2,* which was maintained on a SWR/J background. Timed pregnant mice were euthanized at E7.5-E12.5. Noon on the day of the vaginal plug was considered E0.5 and embryos were staged by counting the number of somites. Analysis of wild-type embryos in Figures 1-3 and associated supplements was performed on FVB/N embryos. Control embryos were wild-type and heterozygous littermate controls of *Ift122*, *Ttc21b,* and *Gli2* mutants (designated WT in the corresponding figures), or embryos bearing Wnt1-Cre2 or SmoM2 alone (designated control in Figure 9 and Figure 9-figure supplements 1 and 2). The presence or absence of exencephaly was analyzed in E10.5-E12.5 embryos. Mutant and transgenic embryos were processed in parallel with littermate controls.

Whole-mount immunostaining

Embryos were dissected in ice-cold PBS and fixed overnight at 4°C in 4-8% paraformaldehyde (PFA, Electron Microscopy Sciences) or Dent's fixative (4:1 methanol:DMSO). Embryos fixed in Dent's fixative were rehydrated in successive 30 min washes of 75:25, 50:50, and 25:75 methanol:PBS at room temperature (RT). Rehydrated embryos were then washed 3 x 30 min in PBS + 0.1% TritonX100 (PBTriton) at RT. Embryos were then incubated in blocking solution (PBS + 3% BSA, 0.1% TritonX100) for 1 h at room temperature. Embryos were then incubated in staining solution (PBS + 1.5% BSA, 0.1% TritonX100) containing primary antibodies overnight at 4°C. Embryos were then washed 3 x 30 min in PBTriton and incubated in staining solution containing Alexa Fluor conjugated secondary antibodies (1:500, ThermoFisher) for 1 h at room temperature. Embryos were subsequently washed 3 x 30 min in PBTriton at RT and stored in PBTriton at 4°C until imaging. Antibodies used for embryos fixed in Dent's fixative were: rat anti-ZO-1 (DSHB R26.4C, 1:100), rabbit anti-Arl13b (Caspary et al., 2007) (1:1,000), rabbit anti-phosphohistone H3 (Upstate 06-570, 1:1,000), and mouse anti-β-catenin (BD Biosciences 610153, 1:300). Antibodies used for embryos fixed in 4% PFA were rabbit anti-laminin (Sigma L9393, 1:1,000), rabbit anti-N-cadherin (Cell Signaling Technology D4R1H, 1:500), chicken anti-GFP (abcam ab13970, 1:1,000), mouse anti-β-catenin (BD Biosciences 610153, 1:300), mouse anti-Nkx6.1 (DSHB F55A10, 1:50), and rabbit anti-FoxA2 (abcam ab108422, 1:1,000). Embryos fixed in 8% PFA were stained with rabbit anti-diphosphomyosin regulatory light chain antibody (Cell Signaling Technology 3674, 1:100). Alexa 546-conjugated phalloidin (Molecular Probes), and DAPI (ThermoFisher) were used as counterstains.

485

486 **Cryosectioning**

487 Embryos were dissected and fixed in 4% PFA for 2 h at room temperature and then washed 5 x
488 30 min in PBTriton. Embryos were then transferred into 15% sucrose for 30 min and
489 subsequently into 30% sucrose overnight at 4°C. Embryos were then placed anterior down in a
490 cryoblock in OCT (Tissue-Tek) and frozen on dry ice. Embryos were stored at -80°C until
491 sectioning. Embryos were sectioned on a cryostat (Leica) from anterior to posterior in 14 µm
492 sections, with sections adsorbed onto Superfrost slides (Fisher). Cryosections from the
493 midbrain/hindbrain region were then washed 3 x 15 min in PBTriton at RT, blocked for 30 min in
494 blocking solution (see above), stained for 30 min with primary antibodies as above, washed 3 x
495 15 min in PBTriton, incubated with secondary antibodies, and washed 3 x 15 min in PBTriton.
496 Stained sections were then mounted under a coverglass in fluorescence mounting media
497 (Dako).

498

499 **Microscopy**

500 For whole-mount confocal analysis, stained embryos were mounted dorsal side down in
501 PBTriton in Attofluor cell chambers (ThermoFisher A7816), using a small fragment of broken
502 coverglass with small dabs of vacuum grease (Dow Corning) to mount the embryo on a #1.5
503 coverglass (Dow Corning). Embryos were then imaged by inverted confocal microscopy on
504 either a Zeiss LSM700 equipped with a Plan-NeoFluar 40x/1.3 oil immersion objective, or a
505 Leica SP8 equipped with a HC PL Apo 40x/1.3 oil immersion objective. Images were captured
506 by tile-based acquisition of contiguous z-stacks of 50-150 µm depth with 0.9-1.2 µm optical
507 slices and 0.3-0.5 µm z-steps. Tiled images were computationally stitched together with 10%
508 overlap per tile using Zen (Zeiss) or LAS-X (Leica) software, resulting in visible seams in some
509 images. Maximum-intensity projections of the entire z depth were created for analysis in the
510 same software. For confocal imaging of cryosections, slides were imaged on an inverted Zeiss
511 LSM700 equipped with a Plan-Apochromat 20x/0.8 air objective. Z-stacks of 10-14 µm depth
512 were imaged with 1.8-2.0 µm optical slices and 1.0-1.2 µm z-steps. For bright-field imaging,
513 embryos were imaged in PBTriton on a Zeiss Stemi 508 stereomicroscope equipped with a
514 Canon EOS DSLR camera and EOS Utility software (Canon).

515

516 **Image analysis and quantification**

517 Apical area was measured in 100 µm x 100 µm regions in maximum-intensity projections of tiled
518 images, either at the midline or in a pair of regions on either side of the midline, approximately

519 midway between the midline and the lateral extent of the neural plate and midway between the
520 pre-otic sulcus and the cranial flexure. For the analysis of cell area throughout the mediolateral
521 axis, a continuous series of 100 μm (anterior-posterior) x 20 μm (mediolateral) regions from the
522 midline to the lateral edge were analyzed. Cells contained entirely within these regions were
523 segmented using SeedWater Segmenter software (Mashburn et al., 2012). Cell areas were
524 quantified and area maps were generated using the MorphoLibJ plugin (Legland et al., 2016) in
525 the FIJI redistribution of ImageJ (Schindelin et al., 2012; Schneider et al., 2012). Cell orientation
526 was evaluated in the same regions using SEGGA software (Farrell et al., 2017). Cells were
527 assigned a mediolateral orientation if they were oriented at 0-45° with respect to the
528 mediolateral axis or an anterior-posterior orientation if they were oriented at 45-90°. Cell height
529 was measured in cryosections by drawing a perpendicular line in FIJI from the apical to the
530 basal surface between two apparent cell edges using phalloidin and laminin or β-catenin (Figure
531 3C-E), or in XZ-reconstructions of embryos stained with phalloidin (Figure 8G and H). The ratio
532 of the apical span to the basal span of the tissue was calculated by manually drawing
533 segmented lines in FIJI from one lateral extreme of the neural plate to the other in cryosections.
534
535 Three-dimensional lateral cell shapes were analyzed using the 3D Project tool in FIJI in cells
536 labeled by EIIA-Cre-driven mosaic recombination of the mT/mG locus, which frequently resulted
537 in individually labeled cells. Cells throughout the lateral midbrain region were analyzed and were
538 manually assigned to shape categories based on examination of their apical, mid- and basal
539 cross-sectional areas. Cells were considered apically constricted if their apical surface was
540 smaller than their basal surface. EIIA-Cre produced little to no labeling in the midline, and
541 midline cell 3D analysis was performed by manual segmentation of cells labeled with β-catenin
542 using ITK-SNAP software (Yushkevich et al., 2006). Comparison of apical and basal areas of
543 midline cells was performed in FIJI.
544
545 For analysis of cell proliferation, the percentage of phosphohistone H3-positive cells was
546 calculated in contiguous 100 μm x 100 μm regions along the mediolateral axis (Figure 4—figure
547 supplement 5) or in a single 100 μm x 100 μm region midway between the midline and the
548 lateral edge of the tissue (Figure 9—figure supplement 1). Mesenchymal cell density was
549 calculated by counting the number of individual DAPI-labeled nuclei in a 50 μm x 100 μm region
550 in transverse sections.
551

552 The number and angle of multicellular F-actin and phosphomyosin cables were analyzed
553 manually using FIJI in a pair of 100 µm x 100 µm lateral regions on either side of the midline in
554 each embryo. A cable was defined as three or more consecutive edges of high-intensity signal
555 with no gap or diminishment along its length. Apical F-actin and phosphomyosin intensity were
556 analyzed in 50 cells in a 50 µm x 50 µm lateral region in embryos stained for phalloidin (F-actin)
557 and phosphorylated myosin II by calculating the mean intensity of a line drawn along the entire
558 apical cortex of each cell. All intensity quantifications were performed on unprocessed maximum
559 intensity projections.
560
561 **Statistics and figure assembly**
562 Statistical analyses and graph generation were performed in Prism software (Graphpad) or with
563 the circular plugin (Agostinelli and Lund, 2017) in the R software package (R Core Team, 2020).
564 All results are reported as mean ± standard deviation (SD). Summary significance levels are as
565 follows: *** $p<0.001$, ** $p<0.01$, * $p<0.05$. Statistical tests were Welch's t-test, which does not
566 assume equal SDs between conditions, the Kolmogorov-Smirnov test for comparing
567 distributions, the standard one-way ANOVA with Tukey's multiple comparisons, which was used
568 when the variance between replicates was expected to come only from measurement error, the
569 Brown-Forsythe and Welch one-way ANOVA using Dunnett's T3 multiple comparisons test,
570 which does not assume equal SDs between conditions, the two-way ANOVA with Sidak's
571 multiple comparisons for comparing multiple conditions, and the Watson nonparametric two-
572 sample test for homogeneity for examining circular distributions. Details of the statistical tests, n
573 values, and p values for each experiment can be found in Supplementary File 1. Figures were
574 assembled using Photoshop and Illustrator (Adobe). For display purposes, some plots did not
575 show cells outside the x-axis range, which were generally <2% of cells, except in Figure 5D
576 (<4% of cells excluded) and Figure 9K (<8% of cells excluded). All cells were included in the
577 statistical analysis. Each embryo was considered a biological replicate. Formal power analyses
578 were not conducted. For mutant analyses, in which mutant embryos were compared with stage-
579 matched littermate controls, an n of 3-5 embryos per genotype was targeted.
580
581 **Acknowledgments**
582 The authors thank Heather Alcorn for identifying and mapping the *Ift122*^{TR2} and *Ttc21b*^{TF2}
583 alleles, Alex Joyner for helpful discussions and for the *Gli2*^{lzki} mice, Ann Sutherland for
584 introducing ERB and JAZ to the mouse neural plate, Ian Prudhomme for technical assistance,
585 and Marissa Gredler, Matthew Schilling, Masako Tamada, and Richard Zallen for comments on

the manuscript. This work was supported by NIH/NINDS F32 fellowship NS098832 to ERB and MSKCC Cancer Center Support Grant P30 CA008748. JAZ is an investigator of the Howard Hughes Medical Institute.

Ethics

Animal experimentation: All animal experiments were conducted in accordance with the Guide for the Care and Use of Laboratory Animals of the National Institutes of Health and an approved Institutional Animal Care and Use Committee (IACUC) protocol (15-08-13) of Memorial Sloan Kettering Cancer Center.

Figure Legends

Figure 1. Lateral cells undergo apical remodeling during cranial neural fold elevation. (**A**) Schematic lateral view of the E8.5 neural plate showing the midbrain and anterior hindbrain region in green. (**B**) Schematic *en face* view of the midbrain and anterior hindbrain region. (**C**) Schematic cross-sectional views of the cranial neural plate during elevation. (**D**) Tiled confocal images of embryos at 0 somites (E7.75) and 6 somites (E8.5) labeled with ZO-1. Midline in center. Arrowhead, pre-otic sulcus. Brackets, regions shown in (**E**). (**E**) Midbrain cells color-coded by apical area. Boxes, regions shown in (**F**). (**F**) Lateral cells at progressive stages of neural fold elevation. Cells are labeled with ZO-1 (top) and are color-coded by apical area (bottom). (**G,H**) Average apical cell area (**G**) and apical area distributions (**H**) of lateral cells during midbrain neural fold elevation. A single value was obtained for each embryo and the mean±SD between embryos is shown, n = 3-6 embryos/stage, **p<0.01, ***p<0.001 (one-way ANOVA test). See Supplementary File 1 for n and p values. Anterior up in (**D-F**). Bars, 100 μm (**D,E**), 20 um (**F**).

Figure 2. Midline cells do not undergo apical remodeling during cranial neural fold elevation. (**A**) Midline cells at progressive stages of neural fold elevation. Cells are labeled with ZO-1 (top) and are color-coded by apical area (bottom). (**B,C**) Average apical cell area (**B**) and apical area distributions (**C**) of midline cells during midbrain neural fold elevation. A single value was obtained for each embryo and the mean±SD between embryos is shown, n = 3 embryos/stage, no significant differences (one-way ANOVA test). See Supplementary File 1 for n and p values. Anterior up. Bar, 20 μm.

Figure 3. Lateral cells, but not midline cells, apically constrict. (**A**) Transverse sections of the cranial neural plate. Phalloidin and laminin show the apical and basal surfaces of the neuroepithelium, respectively. (**B**) The ratio of the apical span to the basal span of the neural plate decreases during elevation, flipping the cranial neural plate from convex (>1) to concave (<1). (**C-E**) Cell height in lateral (**C**) and midline (**D**) regions increases after the 7 somite stage, but the ratio (**E**) does not change. (**F**) Mosaic expression of membrane-GFP using the EIIA-Cre driver. (**G**) 3D projections of membrane-GFP signal from individual lateral cells. (**H**) Midline cells labeled with β-catenin. (**I**) 3D surface renderings of manually segmented midline cells. (**J**) Midbrain neural fold elevation occurs in two phases. Early elevation (0-6 somites) is driven by apical constriction in lateral cells without a change in cell height. At later stages (7-9 somites), both midline and lateral cells undergo significant apicobasal cell elongation. A single value was obtained for each embryo and the mean±SD between embryos is shown, n = 3-4 embryos/stage in (**B-E**), 408 cells in 3 embryos in (**G**), 60 cells in 3 embryos in (**I**), **p<0.01, ***p<0.001 (one-way ANOVA test). See Supplementary File 1 for n and p values. Apical up in (**A**), (**G**), and (**I**), anterior up in (**F**) and (**H**). Bars, 100 μm (**A,F**), 20 μm (**G-I**).

Figure 4. IFT-A proteins have an early role in cranial neural tube closure. (**A**) Wild-type littermate control (WT) showing normal cranial closure. (**B,C**) Exencephaly was observed in 10/10 *Ift122* mutants (B) (compared with 0/16 WT controls) and 5/5 *Ttc21b* mutants (C) (compared with 0/13 WT controls). Dashed lines, lateral edge of the cranial neuroepithelium. (**D-F**) The cranial neural folds fail to elevate in *Ift122* (**E**) and *Ttc21b* (**F**) mutants compared to WT controls (**D**). Box, region shown in (**G-I**). (**G-I**) Lateral cells in WT and mutant embryos. Cells are labeled with ZO-1 (top) and are color-coded by apical area (bottom). (**J-M**) Average apical cell area (**J,L**) and apical area distributions (**K,M**) of lateral cells in *Ift122* and *Ttc21b* mutants compared with WT controls. A single value was obtained for each embryo and the mean±SD between embryos is shown, n = 3-4 embryos/genotype, **p<0.01 (Welch's t-test). See Supplementary File 1 for n and p values. Anterior up in (**A-C**) and (**G-I**), anterior left in (**D-F**). Bars, 1 mm (**A-C**), 100 μm (**D-F**), and 20 μm (**G-I**).

Figure 5. IFT-A mutants display a failure of patterned apical remodeling. (**A**) Schematic of midbrain regions analyzed in (**B**) (blue boxes) and (**F**) (yellow boxes). (**B**) Lateral and midline cells labeled with ZO1 are color-coded by apical area in wild-type littermate control (WT) and *Ift122* mutant embryos. (**C-E**) Apical area distributions (**C,D**) and average apical cell area (**E**). Lateral measurements are reproduced from Figure 4J. (**F**) Contiguous 20 μm wide regions

spanning the mediolateral axis from the midline to the lateral margins of the midbrain neural plate. Cells are labeled with ZO1 and color-coded by apical area. (**G,H**) Apical cell area plotted by distance from the midline. (**I,J**) Average cell height in midline and lateral cells (**I**) measured in transverse sections of the cranial neural plate (**J**). Phalloidin and laminin show apical and basal surfaces, respectively. A single value was obtained for each embryo and the mean±SD between embryos is shown, n = 3-4 embryos/genotype, *p<0.05, **p<0.01 (one-way ANOVA test). See Supplementary File 1 for n and p values. Embryos are anterior up, 7 somites (**B-H**) or apical up, 12 somites (**I,J**). Bars, 20 μm.

Figure 6. Actomyosin organization is disrupted in IFT-A mutants. (**A,E**) Localization of phosphorylated myosin II (phosphomyosin) (A) and F-actin (E) in lateral cells of *Ift122* and *Ttc21b* mutants and wild-type littermate controls (WT). (**B,F**) Orientation of apical phosphomyosin (P-myo) cables (**B**) and F-actin cables (**F**) in *Ift122* and *Ttc21b* mutants and WT controls, Watson two-sample test for homogeneity. (**C,D**) The number of phosphomyosin cables (**C**) and F-actin cables (**D**) per embryo in two 100 μm x 100 μm lateral regions in *Ift122* and *Ttc21b* mutants. (**G,H**) The ratio of phosphomyosin to F-actin at cell-cell junctions was shifted to lower values in *Ttc21b* mutants. A single value was obtained from each embryo and the mean±SD between embryos is shown, n = 29-86 phosphomyosin cables and 100-151 F-actin cables from 3 embryos/genotype in (**A-F**), 50 cells from 3 embryos/genotype (**G,H**), *p<0.05, Welch's t-test in (**C,D**), Watson two-sample test for homogeneity (**B,F**). See Supplementary File 1 for n and p values. Anterior up. Bars, 20 μm.

Figure 7. Shh-dependent cell fates expand laterally in *Ift122* and *Ttc21b* mutants. (**A**) Nkx6.1 protein visualized in tiled confocal images of cranial neural plate cells labeled with phalloidin (F-actin). (**B,C**) Nkx6.1 intensity plotted by distance from the midline, normalized to the mean Nkx6.1 intensity of the image, in *Ift122* (B) and *Ttc21b* (**C**) mutants compared with wild-type littermate controls (WT). A single value was obtained for each embryo and the mean±SD between embryos is shown, n = 3 embryos/genotype. Anterior up. Bars, 100 μm.

Figure 8. Loss of Gli2 disrupts midline but not lateral cell shape. (**A**,**D**) Lateral (**A**) and midline (**D**) cells in *Gli2* mutant embryos and wild-type littermate controls (WT). Cells are labeled with N-cadherin (top) and color coded by apical area (bottom). (**B,C,E,F**) Average apical cell area (**B,E**) and apical area distributions (**C,F**) of lateral and midline cells from WT and *Gli2* mutant embryos. (**G**) XZ reconstructions of lateral and midline cells labeled with F-actin in WT

and *Gli2* mutant embryos. (**H**) Cell height in lateral and midline cells in WT and *Gli2* mutant embryos. A single value was obtained for each embryo and the mean±SD is shown. n = 5 embryos/genotype, **p<0.01, ***p<0.001, Welch's t-test (**B,E**) or Brown-Forsythe one-way ANOVA test (**H**). See Supplementary File 1 for n and p values. Embryos are 7-9 somites. Anterior up in (**A,D**), apical up in (**G**). Bars, 20 μm.

Figure 9. Ectopic Shh signaling disrupts lateral cell remodeling and causes exencephaly. (**A,B**) Expression of the activated Shh receptor Smoothened (SmoM2) using the midbrain-specific Wnt1-Cre2 driver causes exencephaly (12/12 Wnt1-Cre2; SmoM2 embryos vs. 0/13 littermate controls). Control embryos were Wnt1-Cre2 or SmoM2 alone. (**C,D**) Wnt1-Cre2 drives SmoM2-YFP expression in the midbrain and induces ectopic Nkx6.1 expression throughout the mediolateral axis. Boxes, regions shown in (**E,F**). (**E,F**) Cells expressing SmoM2-YFP have larger apical areas compared with cells outside of the Wnt1-Cre2 expression domain (cells below the dashed line) and cells from equivalent regions in controls (**E**). SmoM2-YFP signal at the lateral edge of the N-cadherin region is shown. (**G**) Lateral and midline cells labeled with N-cadherin are color-coded by area in control and SmoM2-expressing embryos. (**H-K**) Average apical cell area (**H,J**) and apical area distributions (**I,K**) in lateral and midline cells in control and SmoM2 embryos. (**L**) Schematics of the pattern and intensity of the Shh response in WT, *Gli2* mutant, IFT-A mutant, and SmoM2-expressing embryos. (**M**) Model. The different shapes of lateral and midline cells correlate with different levels of Shh signaling. A high Shh response inhibits apical remodeling and apicobasal elongation in midline cells, whereas a low Shh response allows apical constriction in lateral cells. A single value was obtained for each embryo and the mean±SD between embryos is shown, n = 3 embryos/genotype, **p<0.01 (Welch's t-test). See Supplementary File 1 for n and p values. Embryos are E10.5 in (**A,B**), 6-7 somites in (**E-K**). Anterior up. Bars, 100 μm in (**C,D**), and 20 μm in (**E**-**G**).

Supplementary Figure Legends

Figure 2 - Supplement 1. Figure 2 - Supplement 1. Analysis of mediolateral cell orientation in midline and lateral cells. (**A,D**) One of the two 100 μm x 100 μm lateral regions analyzed in each wild-type embryo (**A**) and all midline regions analyzed in wild-type embryos (one image/embryo) (**D**) are shown. (**B,E**) Percentage of lateral (**B**) and midline (**E**) cells with a mediolateral (ML) orientation (0-45° relative to the ML axis) or an anterior-posterior (AP)

orientation (45-90° relative to the ML axis) at progressive stages of elevation. (**C,F**) The average ratio of cell length along the ML axis to cell length along the AP axis in lateral (**C**) and midline (**F**) cells. A single value was obtained for each embryo and the mean±SD between embryos is shown. n = 3-6 embryos/stage, *p < 0.05, **p<0.01, ***p<0.001, two-way ANOVA test (**B,E**) or Brown-Forsythe and Welch one-way ANOVA test (**C,F**). See Supplementary File 1 for n and p values. Anterior up. Bars, 20 μm.

Figure 3 - Supplement 1. The cranial neural plate transitions from convex to concave during elevation. (**A**) The apical span of the cranial neural plate decreases significantly during elevation. (**B**) The basal span decreases slightly but does not reach statistical significance. Apical and basal spans were measured from one border to the other in the midbrain neural plate, encompassing midline and lateral cells. A single value was obtained for each embryo and the mean±SD between embryos is shown, n = 3-4 embryos/stage, *p<0.05, **p<0.01 (one-way ANOVA test). See Supplementary File 1 for n and p values.

Figure 3 - Supplement 2. Midline cells do not apically constrict during elevation. (**A**) The apical (top) and basal (bottom) surface of midline cells from a wild-type embryo. Cells outlines are labeled with β-catenin. (**B**) Distributions of the $\log_2$ ratios of the apical area to the basal area of individual cells in three embryos. Cells with positive values are apically expanded, whereas cells with negative values are apically constricted. n = 50 cells/embryo from 3 wild-type embryos. See Supplementary File 1 for n and p values. Anterior up. Bars, 20 μm.

Figure 4 - Supplement 1. Novel *Ift122* and *Ttc21b* alleles have defects in ciliogenesis. (**A,B**) Mouse *Ift122* (A) and *Ttc21b* (B) loci showing the *Ift122*^{TR2} and *Ttc21b*^{TF2} mutations. (**C-E**) Localization of ZO-1 and the cilia marker Arl13b in lateral cells of the midbrain neural plate at 7-8 somites. Note the reduction in Arl13b staining in *Ift122* and *Ttc21b*. Anterior up. Bar, 20 μm.

Figure 4 - Supplement 2. *Ift122* and *Ttc21b* mutants display a persistent failure of neural fold elevation. (**A-C'**) *Ift122* and *Ttc21b* embryos at 7 somites compared with a wild-type (WT) littermate control. Top panels, side views. Bottom panels, ventral views. Note the failure of neural fold elevation in *Ift122* and *Ttc21b* mutants. POS, pre-otic sulcus; OS, otic sulcus. Anterior left. (**D-E'**) *Ift122* embryos at 12 somites compared with a WT littermate control. Top panels, dorsal views. Bottom panels, frontal views. Lateral neural folds are unelevated in the *Ift122* mutant midbrain and forebrain. (**F-G'**) *Ift122* embryos at E9.5 compared with a WT

littermate control. Top panels, side views. Bottom panels, dorsal views. Cranial closure is completed by E9.5 in WT but the midbrain and forebrain neural folds are unelevated in *Ift122* mutants. Dashed lines indicate the lateral neural plate borders.

Figure 4 - Supplement 3. Disrupted cranial architecture in *Ift122* mutants. (**A-D**) Serial transverse sections through a wild-type littermate control (WT) and an *Ift122* mutant embryo at 11 somites. Phalloidin and laminin label the apical and basal surfaces of the neuroepithelium, respectively. Nkx6.1 labels ventral cells. In WT, the forebrain (fb, white arrowhead in top panel) is closed and the midbrain (mb) displays substantial neural fold elevation. In contrast, the *Ift122* mutant shows a failure of forebrain closure (yellow arrowheads in top panel). Asterisks indicate the connection between the dorsal aorta and the first brachial arch artery. Nkx6.1 signal in the foregut pocket (f) is nonspecific trapping of secondary antibody. Bars, 100 μm.

Figure 4 - Supplement 4. Analysis of mediolateral cell orientation in *Ift122* and *Ttc21b* mutants. (**A,C**) Percentage of lateral cells (A) and midline cells (C) with a mediolateral (ML) orientation (0-45° relative to the ML axis) or an anterior-posterior (AP) orientation (45-90° relative to the ML axis) in *Ift122* mutants and wild-type littermate controls (WT). (**B,D**) Average ratio of cell length along the ML and AP axes. **(E**) Percentage of lateral cells with an ML or AP orientation in *Ttc21b* mutants and WT littermate controls. (**F**) Average ratio of cell length along the ML and AP axes. Midline cells could not be analyzed due to deep midline folds in *Ttc21b* mutants. A single value was obtained for each embryo and the mean±SD between embryos is shown. n = 3-4 embryos/genotype, *p < 0.05, ** p < 0.01, two-way ANOVA test (**A,C,E**) or Welch's t-test (**B,D,F**). See Supplementary File 1 for n and p values.

Figure 4 - Supplement 5. Cell proliferation is not affected in *Ift122* and *Ttc21b* mutants. (**A**) Images of the cranial neuroepithelium from the midbrain at the level of the cranial flexure (top) to the closed hindbrain (bottom) in a wild-type littermate control (WT) and an *Ift122* mutant. Dividing cells are labeled with phospho-histone H3 (pHH3), which labels cells in M phase. Dashed rectangles indicate regions analyzed in (**E**). (**B**) Projections of the cranial neuroepithelium from the forebrain-midbrain border (top) to the midbrain-hindbrain border (bottom) showing M-phase cells labeled with pHH3. Dashed rectangles indicate regions analyzed in (**F**). (**C,D**) Lateral cells in *Ift122* (**C**) and *Ttc21b* (**D**) mutants and littermate controls labeled with pHH3 and ZO-1. (**E,F**) The percentage of proliferative (pHH3+) cells in 100 μm x 100 μm regions plotted by distance from the midline. Each bin is plotted at the minimum

distance for that bin. A single value was obtained for each embryo and the mean±SD between embryos is shown, n = 3 embryos/genotype. No significant differences were observed between mutant embryos and WT controls (two-way ANOVA test). See Supplementary File 1 for n and p values. Anterior up. Bars, 100 μm (**A,B**), 20 μm (**C,D**).

Figure 4 - Supplement 6. Mesenchymal cell density is not affected in *Ttc21b* mutants. (**A**) Cell nuclei visualized with DAPI in the plane of the mesenchymal cells underlying the cranial neural plate from transverse sections of individual embryos. (**B**) The number of mesenchymal cells per 50 μm x 100 μm region is plotted for *Ttc21b* mutants and wild-type littermate controls (WT). A single value was obtained for each embryo and the mean±SD between embryos is shown, n = 3 embryos/genotype, Welch's t-test. No significant differences between genotypes were observed. See Supplementary File 1 for n and p values. Apical up. Bar, 20 μm.

Figure 5 - Supplement 1. The convex to concave transition is defective in *Ift122* and *Ttc21b* mutants. (**A**) Transverse sections of a *Ttc21b* mutant and a wild-type littermate control (WT) at 8 somites. Phalloidin and laminin label the apical and basal surfaces of the neuroepithelium, respectively. DAPI (white) shows the nuclei. (**B**) Midline cells are significantly shorter than lateral cells in WT controls at 8 somites. This difference is eliminated in *Ttc21b* mutants. (**C-F**) The ratio of the apical span to the basal span of the neuroepithelium is increased in *Ttc21b* mutants at mid-elevation (8-9 somites) (**C,D**) and in *Ift122* mutants at late elevation (12 somites) (**E,F**). Apical and basal spans were measured from one border to the other, encompassing midline and lateral cells. A single value was obtained for each embryo and the mean±SD between embryos is shown, n = 3 embryos/genotype, *p<0.05, **p<0.01 (one-way ANOVA test in **B**, Welch's t-test in **C-F**). See Supplementary File 1 for n and p values. Apical up. Bars, 20 μm.

Figure 8 – Supplement 1. Gli2 is required for FoxA2 expression in the ventral neural plate. (**A**) Single z-planes of *Gli2* mutant and wild-type littermate control (WT) embryos at the level of the floor plate of the midbrain neural plate (top) or at the level of the underlying notochord (bottom) labeled with the ventral/floor plate marker FoxA2 and counterstained with phalloidin (F-actin). Note that FoxA2 is expressed in the notochord but not the floor plate of *Gli2* mutants. (**B**) Maximum-intensity projections of WT control and *Gli2* mutant neural plates labeled with the ventral marker Nkx6.1 and phalloidin. Embryos are 7-8 somites. Anterior up. Bars, 100 μm.

Figure 8 - Supplement 2. Analysis of mediolateral cell orientation in *Gli2* mutants. (**A,C**) Percentage of lateral cells (A) and midline cells (C) with a mediolateral (ML) orientation (0-45° relative to the ML axis) or an anterior-posterior (AP) orientation (45-90° relative to the ML axis) in *Gli2* mutants and wild-type littermate controls (WT). (**B,D**) Average ratio of cell length along the ML and AP axes. n = 5 embryos/genotype, two-way ANOVA test (A,C) or Welch's t-test (B,D). See Supplementary File 1 for n and p values.

Figure 9 – Supplement 1. Cell proliferation is not affected by neuroepithelial expression of SmoM2. (**A**) Lateral cell proliferation in embryos labeled with pHH3 to mark mitotic cells and phalloidin (F-actin) to mark cell outlines in embryos expressing activated Smoothened using the midbrain-specific Wnt1-Cre driver. Control embryos were Wnt1-Cre2 or SmoM2 alone. (**B**) The percentage of proliferative (pHH3+) cells in a 100 μm x 100 μm lateral region. No significant difference was observed between SmoM2-expressing embryos and controls. A single value was obtained for each embryo and the mean±SD between embryos is shown, n = 4 embryos/genotype, Welch's t-test. Embryos are 7-9 somites. See Supplementary File 1 for n and p values. Anterior up. Bars, 20 μm.

Figure 9 - Supplement 2. Analysis of mediolateral cell orientation in SmoM2-expressing embryos. (**A,C**) Percentage of lateral cells (A) and midline cells (C) with a mediolateral (ML) orientation (0-45° relative to the ML axis) or an anterior-posterior (AP) orientation (45-90° relative to the ML axis) in embryos expressing activated Smoothened using the midbrain-specific Wnt1-Cre2 driver. Control embryos were Wnt1-Cre2 or SmoM2 alone. (**B,D**) Average ratio of cell length along the ML and AP axes. n = 3 embryos per genotype, two-way ANOVA test (A,C) or Welch's t-test (B,D). See Supplementary File 1 for n and p values.

Supplementary File 1. N values and details of statistical analyses performed. The details of the statistical tests performed, including the exact n and p values in the Figures and Figure supplements are presented.

858 **References**

859

860 Agostinelli C, Lund U. 2017. R package circular: Circular Statistics (version 0.4-93).
861 Arraf AA, Yelin R, Reshef I, Jadon J, Abboud M, Zaher M, Schneider J, Vladimirov FK,
862 Schultheiss TM. 2020. Hedgehog Signaling Regulates Epithelial Morphogenesis to
863 Position the Ventral Embryonic Midline. *Dev Cell* **53**:589-602.
864 Aw WY, Devenport D. 2017. Planar cell polarity: global inputs establishing cellular asymmetry.
865 *Curr Opin Cell Biol* **44**:110–116.
866 Bai CB, Auerbach W, Lee JS, Stephen D, Joyner AL. 2002. Gli2, but not Gli1, is required for
867 initial Shh signaling and ectopic activation of the Shh pathway. *Development* **129**:4753–
868 4761.
869 Bangs F, Anderson KV. 2017. Primary Cilia and Mammalian Hedgehog Signaling. *Cold Spring*
870 *Harb Perspect Biol* **9**. doi:10.1101/cshperspect.a028175
871 Brouns MR, Matheson SF, Hu KQ, Delalle I, Caviness VS, Silver J, Bronson RT, Settleman J.
872 2000. The adhesion signaling molecule p190 RhoGAP is required for morphogenetic
873 processes in neural development. *Development* **127**:4891–4903.
874 Brunet T, Larson BT, Linden TA, Vermeij MJA, McDonald K, King N. 2019. Light-regulated
875 collective contractility in a multicellular choanoflagellate. *Science* **366**:326–334.
876 Burnside B. 1973. Microtubules and Microfilaments in Amphibian Neurulation. *Integr Comp Biol*
877 **13**:989–1006.
878 Burnside MB, Jacobson AG. 1968. Analysis of morphogenetic movements in the neural plate of
879 the newt *Taricha torosa*. *Dev Biol* **18**:537–552.
880 Cameron DA, Pennimpede T, Petkovich M. 2009. Tulp3 is a critical repressor of mouse
881 hedgehog signaling. *Dev Dyn* **238**:1140–1149.
882 Caspary T, Larkins CE, Anderson KV. 2007. The graded response to Sonic Hedgehog depends
883 on cilia architecture. *Dev Cell* **12**:767–778.
884 Corrigall D, Walther RF, Rodriguez L, Fichelson P, Pichaud F. 2007. Hedgehog signaling is a
885 principal inducer of Myosin-II-driven cell ingression in *Drosophila* epithelia. *Dev Cell*
886 **13**:730–742.
887 Cortellino S, Wang C, Wang B, Bassi MR, Caretti E, Champeval D, Calmont A, Jarnik M, Burch
888 J, Zaret KS, Larue L, Bellacosa A. 2009. Defective ciliogenesis, embryonic lethality and
889 severe impairment of the Sonic Hedgehog pathway caused by inactivation of the mouse
890 complex A intraflagellar transport gene *Ift122/Wdr10*, partially overlapping with the DNA
891 repair gene *Med1/Mbd4*. *Dev Biol* **325**:225–237.
892 Davidson LA, Keller RE. 1999. Neural tube closure in *Xenopus laevis* involves medial migration,
893 directed protrusive activity, cell intercalation and convergent extension. *Development*
894 **126**:4547–4556.
895 Dessaud E, McMahon AP, Briscoe J. 2008. Pattern formation in the vertebrate neural tube: a
896 sonic hedgehog morphogen-regulated transcriptional network. *Development* **135**:2489–
897 2503.
898 Eom DS, Amarnath S, Fogel JL, Agarwala S. 2011. Bone morphogenetic proteins regulate
899 neural tube closure by interacting with the apicobasal polarity pathway. *Development*
900 **138**:3179–3188.
901 Escudero LM, Bischoff M, Freeman M. 2007. Myosin II regulates complex cellular arrangement
902 and epithelial architecture in *Drosophila*. *Dev Cell* **13**:717–729.
903 Escuin S, Vernay B, Savery D, Gurniak CB, Witke W, Greene NDE, Copp AJ. 2015. Rho-
904 kinase-dependent actin turnover and actomyosin disassembly are necessary for mouse
905 spinal neural tube closure. *J Cell Sci* **128**:2468–2481.
906 Farrell DL, Weitz O, Magnasco MO, Zallen JA. 2017. SEGGA: a toolset for rapid automated
907 analysis of epithelial cell polarity and dynamics. *Development* **144**:1725–1734.

908 Fournier-Thibault C, Blavet C, Jarov A, Bajanca F, Thorsteinsdóttir S, Duband J-L. 2009. Sonic
909 hedgehog regulates integrin activity, cadherin contacts, and cell polarity to orchestrate
910 neural tube morphogenesis. *J Neurosci* **29**:12506–12520.
911 García-García MJ, Eggenschwiler JT, Caspary T, Alcorn HL, Wyler MR, Huangfu D, Rakeman
912 AS, Lee JD, Feinberg EH, Timmer JR, Anderson KV. 2005. Analysis of mouse
913 embryonic patterning and morphogenesis by forward genetics. *Proc Natl Acad Sci U S A*
914 **102**:5913–5919.
915 Gordon HB, Lusk S, Carney KR, Wirick EO, Murray BF, Kwan KM. 2018. Hedgehog signaling
916 regulates cell motility and optic fissure and stalk formation during vertebrate eye
917 morphogenesis. *Development* **145**. doi:10.1242/dev.165068
918 Grego-Bessa J, Bloomekatz J, Castel P, Omelchenko T, Baselga J, Anderson KV. 2016. The
919 tumor suppressor PTEN and the PDK1 kinase regulate formation of the columnar neural
920 epithelium. *eLife* **5**:e12034.
921 Grego-Bessa J, Hildebrand J, Anderson KV. 2015. Morphogenesis of the mouse neural plate
922 depends on distinct roles of cofilin 1 in apical and basal epithelial domains. *Development*
923 **142**:1305–1314.
924 Haigo SL, Hildebrand JD, Harland RM, Wallingford JB. 2003. Shroom induces apical
925 constriction and is required for hingepoint formation during neural tube closure. *Curr Biol*
926 **13**:2125–2137.
927 Harris MJ, Juriloff DM. 2007. Mouse mutants with neural tube closure defects and their role in
928 understanding human neural tube defects. *Birth Defects Res A Clin Mol Teratol* **79**:187–
929 210.
930 Harris MJ, Juriloff DM. 2010. An update to the list of mouse mutants with neural tube closure
931 defects and advances toward a complete genetic perspective of neural tube closure.
932 *Birth Defects Res A Clin Mol Teratol* **88**:653–669.
933 Hashimoto H, Robin FB, Sherrard KM, Munro EM. 2015. Sequential contraction and exchange
934 of apical junctions drives zippering and neural tube closure in a simple chordate. *Dev*
935 *Cell* **32**:241–255.
936 Hildebrand JD, Soriano P. 1999. Shroom, a PDZ Domain–Containing Actin-Binding Protein, Is
937 Required for Neural Tube Morphogenesis in Mice. *Cell* **99**:485–497.
938 Hui CC, Joyner AL. 1993. A mouse model of greig cephalopolysyndactyly syndrome: the *extra-*
939 *toesJ* mutation contains an intragenic deletion of the *Gli3* gene. *Nat Genet* **3**:241–246.
940 Ikeda A, Ikeda S, Gridley T, Nishina PM, Naggert JK. 2001. Neural tube defects and
941 neuroepithelial cell death in *Tulp3* knockout mice. *Hum Mol Genet* **10**:1325–1334.
942 Itoh K, Ossipova O, Sokol SY. 2014. GEF-H1 functions in apical constriction and cell
943 intercalations and is essential for vertebrate neural tube closure. *J Cell Sci* **127**:2542–
944 2553.
945 Jacobson AG, Tam PP. 1982. Cephalic neurulation in the mouse embryo analyzed by SEM and
946 morphometry. *Anat Rec* **203**:375–396.
947 Jeong J, Mao J, Tenzen T, Kottmann AH, McMahon AP. 2004. Hedgehog signaling in the
948 neural crest cells regulates the patterning and growth of facial primordia. *Genes Dev*
949 **18**:937–951.
950 Jessell TM. 2000. Neuronal specification in the spinal cord: inductive signals and transcriptional
951 codes. *Nat Rev Genet* **1**:20–29.
952 Juriloff DM, Harris MJ. 2018. Insights into the Etiology of Mammalian Neural Tube Closure
953 Defects from Developmental, Genetic and Evolutionary Studies. *J Dev Biol* **6**:22.
954 Keller RE. 1981. An experimental analysis of the role of bottle cells and the deep marginal zone
955 in gastrulation of *Xenopus laevis*. *J Exp Zool* **216**:81–101.
956 Kicheva A, Briscoe J. 2015. Developmental Pattern Formation in Phases. *Trends Cell Biol*
957 **25**:579–591.

Ko CS, Martin AC. 2020. The cellular and molecular mechanisms that establish the mechanics of *Drosophila* gastrulation. *Curr Top Dev Biol* **136**:141–165.

Lakso M, Pichel JG, Gorman JR, Sauer B, Okamoto Y, Lee E, Alt FW, Westphal H. 1996. Efficient in vivo manipulation of mouse genomic sequences at the zygote stage. *Proc Natl Acad Sci U S A* **93**:5860–5865.

Lee C, Scherr HM, Wallingford JB. 2007. Shroom family proteins regulate gamma-tubulin distribution and microtubule architecture during epithelial cell shape change. *Development* **134**:1431–1441.

Lee J-Y, Goldstein B. 2003. Mechanisms of cell positioning during *C. elegans* gastrulation. *Development* **130**:307–320.

Lee J-Y, Harland RM. 2007. Actomyosin contractility and microtubules drive apical constriction in *Xenopus* bottle cells. *Dev Biol* **311**:40–52.

Lee J-Y, Harland RM. 2010. Endocytosis is required for efficient apical constriction during *Xenopus* gastrulation. *Curr Biol* **20**:253–258.

Lee J-Y, Marston DJ, Walston T, Hardin J, Halberstadt A, Goldstein B. 2006. Wnt/Frizzled signaling controls *C. elegans* gastrulation by activating actomyosin contractility. *Curr Biol* **16**:1986–1997.

Legland D, Arganda-Carreras I, Andrey P. 2016. MorphoLibJ: integrated library and plugins for mathematical morphology with ImageJ. *Bioinformatics* **32**:3532–3534.

Lewis AE, Vasudevan HN, O'Neill AK, Soriano P, Bush JO. 2013. The widely used *Wnt1-Cre* transgene causes developmental phenotypes by ectopic activation of Wnt signaling. *Dev Biol* **379**:229–234.

Liem KF Jr, Ashe A, He M, Satir P, Moran J, Beier D, Wicking C, Anderson KV. 2012. The IFT-A complex regulates Shh signaling through cilia structure and membrane protein trafficking. *J Cell Biol* **197**:789–800.

Martin AC, Goldstein B. 2014. Apical constriction: themes and variations on a cellular mechanism driving morphogenesis. *Development* **141**:1987–1998.

Mashburn DN, Lynch HE, Ma X, Hutson MS. 2012. Enabling user-guided segmentation and tracking of surface-labeled cells in time-lapse image sets of living tissues. *Cytometry A* **81**:409–418.

Massarwa R, Ray HJ, Niswander L. 2014. Morphogenetic movements in the neural plate and neural tube: mouse. *Wiley Interdiscip Rev Dev Biol* **3**:59–68.

Matise MP, Epstein DJ, Park HL, Platt KA, Joyner AL. 1998. Gli2 is required for induction of floor plate and adjacent cells, but not most ventral neurons in the mouse central nervous system. *Development* **125**:2759–2770.

McGlinn E, Tabin CJ. 2006. Mechanistic insight into how Shh patterns the vertebrate limb. *Curr Opin Genet Dev* **16**:426–432.

McGreevy EM, Vijayraghavan D, Davidson LA, Hildebrand JD. 2015. Shroom3 functions downstream of planar cell polarity to regulate myosin II distribution and cellular organization during neural tube closure. *Biol Open* **4**:186–196.

McMahon AP, Ingham PW, Tabin CJ. 2003. Developmental roles and clinical significance of hedgehog signaling. *Curr Top Dev Biol* **53**:1–114.

McShane SG, Molè MA, Savery D, Greene NDE, Tam PPL, Copp AJ. 2015. Cellular basis of neuroepithelial bending during mouse spinal neural tube closure. *Dev Biol* **404**:113–124.

Mo R, Freer AM, Zinyk DL, Crackower MA, Michaud J, Heng HH, Chik KW, Shi XM, Tsui LC, Cheng SH, Joyner AL, Hui C. 1997. Specific and redundant functions of Gli2 and Gli3 zinc finger genes in skeletal patterning and development. *Development* **124**:113–123.

Molè MA, Galea GL, Rolo A, Weberling A, Nychyk O, De Castro SC, Savery D, Fässler R, Ybot-González P, Greene NDE, Copp AJ. 2020. Integrin-Mediated Focal Anchorage Drives Epithelial Zippering during Mouse Neural Tube Closure. *Dev Cell* **52**:321-334.e6.

1008 Morriss-Kay G, Tuckett F. 1985. The role of microfilaments in cranial neurulation in rat embryos:
1009 effects of short-term exposure to cytochalasin D. *J Embryol Exp Morphol* **88**:333–348.
1010 Murdoch JN, Copp AJ. 2010. The relationship between sonic Hedgehog signaling, cilia, and
1011 neural tube defects. *Birth Defects Res A Clin Mol Teratol* **88**:633–652.
1012 Muzumdar MD, Tasic B, Miyamichi K, Li L, Luo L. 2007. A global double-fluorescent Cre
1013 reporter mouse. *Genesis* **45**:593–605.
1014 Nasr T, Mancini P, Rankin SA, Edwards NA, Agricola ZN, Kenny AP, Kinney JL, Daniels K,
1015 Vardanyan J, Han L, Trisno SL, Cha S-W, Wells JM, Kofron MJ, Zorn AM. 2019.
1016 Endosome-Mediated Epithelial Remodeling Downstream of Hedgehog-Gli Is Required
1017 for Tracheoesophageal Separation. *Dev Cell* **51**:665-674.e6.
1018 Nikolopoulou E, Galea GL, Rolo A, Greene NDE, Copp AJ. 2017. Neural tube closure: cellular,
1019 molecular and biomechanical mechanisms. *Development* **144**:552–566.
1020 Nishimura T, Honda H, Takeichi M. 2012. Planar cell polarity links axes of spatial dynamics in
1021 neural-tube closure. *Cell* **149**:1084–1097.
1022 Nishimura T, Takeichi M. 2008. Shroom3-mediated recruitment of Rho kinases to the apical cell
1023 junctions regulates epithelial and neuroepithelial planar remodeling. *Development*
1024 **135**:1493–1502.
1025 Norman RX, Ko HW, Huang V, Eun CM, Abler LL, Zhang Z, Sun X, Eggenschwiler JT. 2009.
1026 Tubby-like protein 3 (TULP3) regulates patterning in the mouse embryo through
1027 inhibition of Hedgehog signaling. *Hum Mol Genet* **18**:1740–1754.
1028 Ohmura T, Shioi G, Hirano M, Aizawa S. 2012. Neural tube defects by *NUAK1* and *NUAK2*
1029 double mutation. *Dev Dyn* **241**:1350–1364.
1030 Ossipova O, Kim K, Lake BB, Itoh K, Ioannou A, Sokol SY. 2014. Role of Rab11 in planar cell
1031 polarity and apical constriction during vertebrate neural tube closure. *Nat Commun*
1032 **5**:3734.
1033 Patterson VL, Damrau C, Paudyal A, Reeve B, Grimes DT, Stewart ME, Williams DJ, Siggers P,
1034 Greenfield A, Murdoch JN. 2009. Mouse *hitchhiker* mutants have spina bifida, dorso-
1035 ventral patterning defects and polydactyly: identification of Tulp3 as a novel negative
1036 regulator of the Sonic hedgehog pathway. *Hum Mol Genet* **18**:1719–1739.
1037 Plageman TF Jr, Chung M-I, Lou M, Smith AN, Hildebrand JD, Wallingford JB, Lang RA. 2010.
1038 Pax6-dependent *Shroom3* expression regulates apical constriction during lens placode
1039 invagination. *Development* **137**:405–415.
1040 Pyrgaki C, Trainor P, Hadjantonakis A-K, Niswander L. 2010. Dynamic imaging of mammalian
1041 neural tube closure. *Dev Biol* **344**:941–947.
1042 Qin J, Lin Y, Norman RX, Ko HW, Eggenschwiler JT. 2011. Intraflagellar transport protein 122
1043 antagonizes Sonic Hedgehog signaling and controls ciliary localization of pathway
1044 components. *Proc Natl Acad Sci U S A* **108**:1456–1461.
1045 Qiu M, Shimamura K, Sussel L, Chen S, Rubenstein JL. 1998. Control of anteroposterior and
1046 dorsoventral domains of *Nkx-6.1* gene expression relative to other *Nkx* genes during
1047 vertebrate CNS development. *Mech Dev* **72**:77–88.
1048 R Core Team. 2020. R: A Language and Environment for Statistical Computing.
1049 Rao-Bhatia A, Zhu M, Yin W-C, Coquenlorge S, Zhang X, Woo J, Sun Y, Dean CH, Liu A, Hui
1050 C-C, Shivdasani RA, McNeill H, Hopyan S, Kim T-H. 2020. Hedgehog-Activated Fat4
1051 and PCP Pathways Mediate Mesenchymal Cell Clustering and Villus Formation in Gut
1052 Development. *Dev Cell* **52**:647-658.e6.
1053 Ray HJ, Niswander LA. 2016a. Dynamic behaviors of the non-neural ectoderm during
1054 mammalian cranial neural tube closure. *Dev Biol* **416**:279–285.
1055 Ray HJ, Niswander LA. 2016b. Grainyhead-like 2 downstream targets act to suppress epithelial-
1056 to-mesenchymal transition during neural tube closure. *Development* **143**:1192–1204.
1057 Robbins DJ, Fei DL, Riobo NA. 2012. The Hedgehog signal transduction network. *Sci Signal*
1058 **5**:re6.

de la Roche M, Ritter AT, Angus KL, Dinsmore C, Earnshaw CH, Reiter JF, Griffiths GM. 2013. Hedgehog signaling controls T cell killing at the immunological synapse. *Science* **342**:1247–1250.

Sagner A, Briscoe J. 2019. Establishing neuronal diversity in the spinal cord: a time and a place. *Development* **146**. doi:10.1242/dev.182154.

Schindelin J, Arganda-Carreras I, Frise E, Kaynig V, Longair M, Pietzsch T, Preibisch S, Rueden C, Saalfeld S, Schmid B, Tinevez J-Y, White DJ, Hartenstein V, Eliceiri K, Tomancak P, Cardona A. 2012. Fiji: an open-source platform for biological-image analysis. *Nat Methods* **9**:676–682.

Schneider CA, Rasband WS, Eliceiri KW. 2012. NIH Image to ImageJ: 25 years of image analysis. *Nat Methods* **9**:671–675.

Schoenwolf GC, Franks MV. 1984. Quantitative analyses of changes in cell shapes during bending of the avian neural plate. *Dev Biol* **105**:257–272.

Smith JL, Schoenwolf GC. 1988. Role of cell-cycle in regulating neuroepithelial cell shape during bending of the chick neural plate. *Cell Tissue Res* **252**:491–500.

Smith JL, Schoenwolf GC, Quan J. 1994. Quantitative analyses of neuroepithelial cell shapes during bending of the mouse neural plate. *J Comp Neurol* **342**:144–151.

Stottmann RW, Berrong M, Matta K, Choi M, Klingensmith J. 2006. The BMP antagonist Noggin promotes cranial and spinal neurulation by distinct mechanisms. *Dev Biol* **295**:647–663.

Sutherland A, Keller R, Lesko A. 2020. Convergent extension in mammalian morphogenesis. *Semin Cell Dev Biol* **100**:199-211.

Svärd J, Heby-Henricson K, Persson-Lek M, Rozell B, Lauth M, Bergström A, Ericson J, Toftgård R, Teglund S. 2006. Genetic elimination of Suppressor of fused reveals an essential repressor function in the mammalian Hedgehog signaling pathway. *Dev Cell* **10**:187–197.

Tang M, Luo SX, Tang V, Huang EJ. 2013. Temporal and spatial requirements of Smoothened in ventral midbrain neuronal development. *Neural Dev* **8**:8.

Tickle C, Towers M. 2017. Sonic Hedgehog Signaling in Limb Development. *Front Cell Dev Biol* **5**:14.

Tran PV, Haycraft CJ, Besschetnova TY, Turbe-Doan A, Stottmann RW, Herron BJ, Chesebro AL, Qiu H, Scherz PJ, Shah JV, Yoder BK, Beier DR. 2008. THM1 negatively modulates mouse sonic hedgehog signal transduction and affects retrograde intraflagellar transport in cilia. *Nat Genet* **40**:403–410.

Vijayraghavan DS, Davidson LA. 2017. Mechanics of neurulation: From classical to current perspectives on the physical mechanics that shape, fold, and form the neural tube. *Birth Defects Res* **109**:153–168.

Villavicencio EH, Walterhouse DO, Iannaccone PM. 2000. The sonic hedgehog-patched-gli pathway in human development and disease. *Am J Hum Genet* **67**:1047–1054.

Wallingford JB, Harland RM. 2002. Neural tube closure requires Dishevelled-dependent convergent extension of the midline. *Development* **129**:5815–5825.

Wallingford JB, Niswander LA, Shaw GM, Finnell RH. 2013. The continuing challenge of understanding, preventing, and treating neural tube defects. *Science* **339**:1222002.

Wilde JJ, Petersen JR, Niswander L. 2014. Genetic, epigenetic, and environmental contributions to neural tube closure. *Annu Rev Genet* **48**:583–611.

Williams M, Yen W, Lu X, Sutherland A. 2014. Distinct apical and basolateral mechanisms drive planar cell polarity-dependent convergent extension of the mouse neural plate. *Dev Cell* **29**:34–46.

Wong SY, Reiter JF. 2008. The primary cilium at the crossroads of mammalian hedgehog signaling. *Curr Top Dev Biol* **85**:225–260.

Ybot-Gonzalez P, Cogram P, Gerrelli D, Copp AJ. 2002. Sonic hedgehog and the molecular regulation of mouse neural tube closure. *Development* **129**:2507–2517.

1110 Ybot-Gonzalez P, Copp AJ. 1999. Bending of the neural plate during mouse spinal neurulation
1111 is independent of actin microfilaments. *Dev Dyn* **215**:273–283.
1112 Ybot-Gonzalez P, Gaston-Massuet C, Girdler G, Klingensmith J, Arkell R, Greene NDE, Copp
1113 AJ. 2007. Neural plate morphogenesis during mouse neurulation is regulated by
1114 antagonism of Bmp signalling. *Development* **134**:3203–3211.
1115 Yushkevich PA, Piven J, Hazlett HC, Smith RG, Ho S, Gee JC, Gerig G. 2006. User-guided 3D
1116 active contour segmentation of anatomical structures: significantly improved efficiency
1117 and reliability. *Neuroimage* **31**:1116–1128.
1118 Zaganjor I, Sekkarie A, Tsang BL, Williams J, Razzaghi H, Mulinare J, Sniezek JE, Cannon MJ,
1119 Rosenthal J. 2016. Describing the Prevalence of Neural Tube Defects Worldwide: A
1120 Systematic Literature Review. *PLoS One* **11**:e0151586.
1121 Zuñiga NR, Stoeckli ET. 2017. Sonic -'Jack-of-all-trades' in neural circuit formation. *J Dev Biol*
1122 **5**. doi:10.3390/jdb5010002.

Figure 1

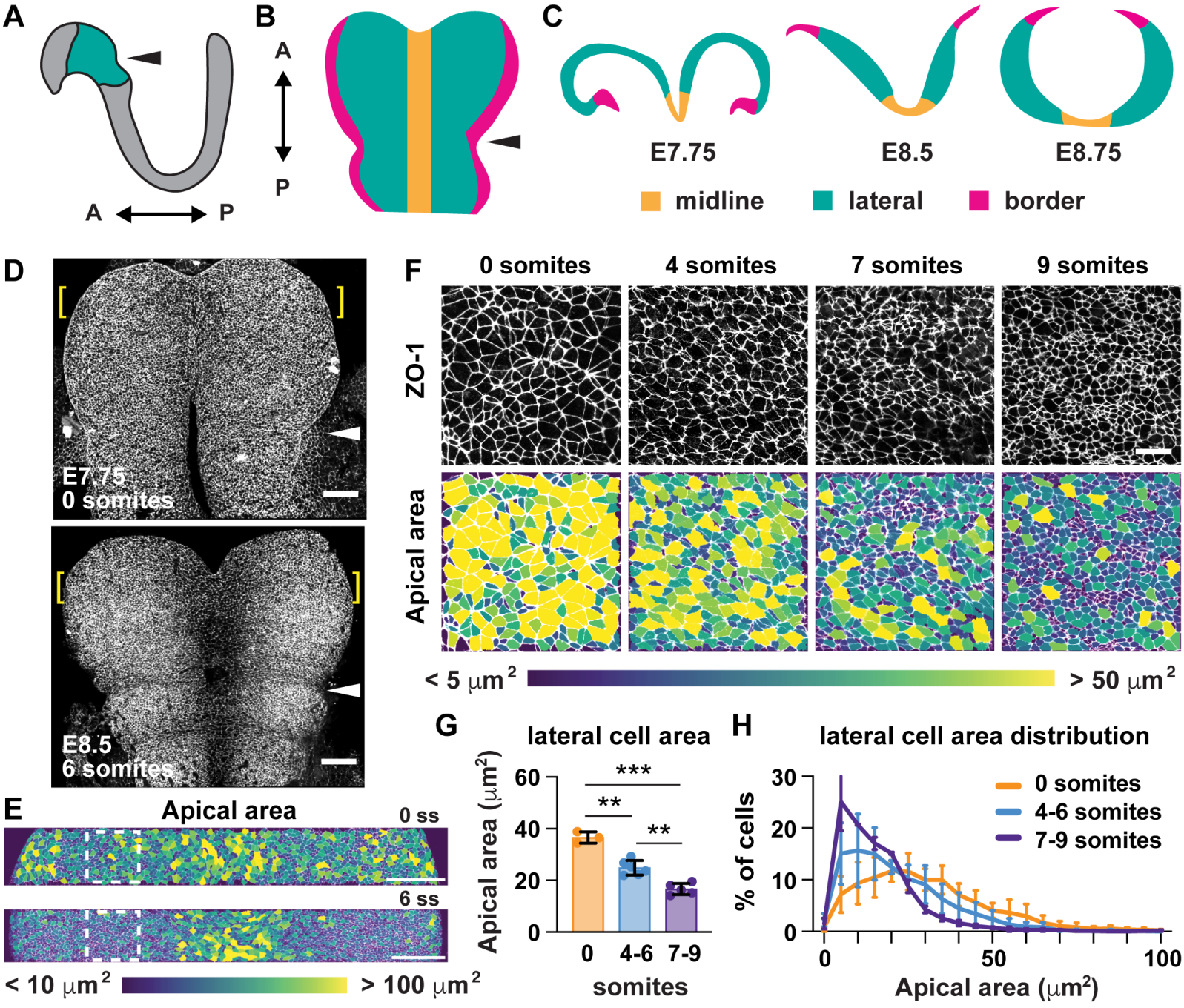

Figure 2

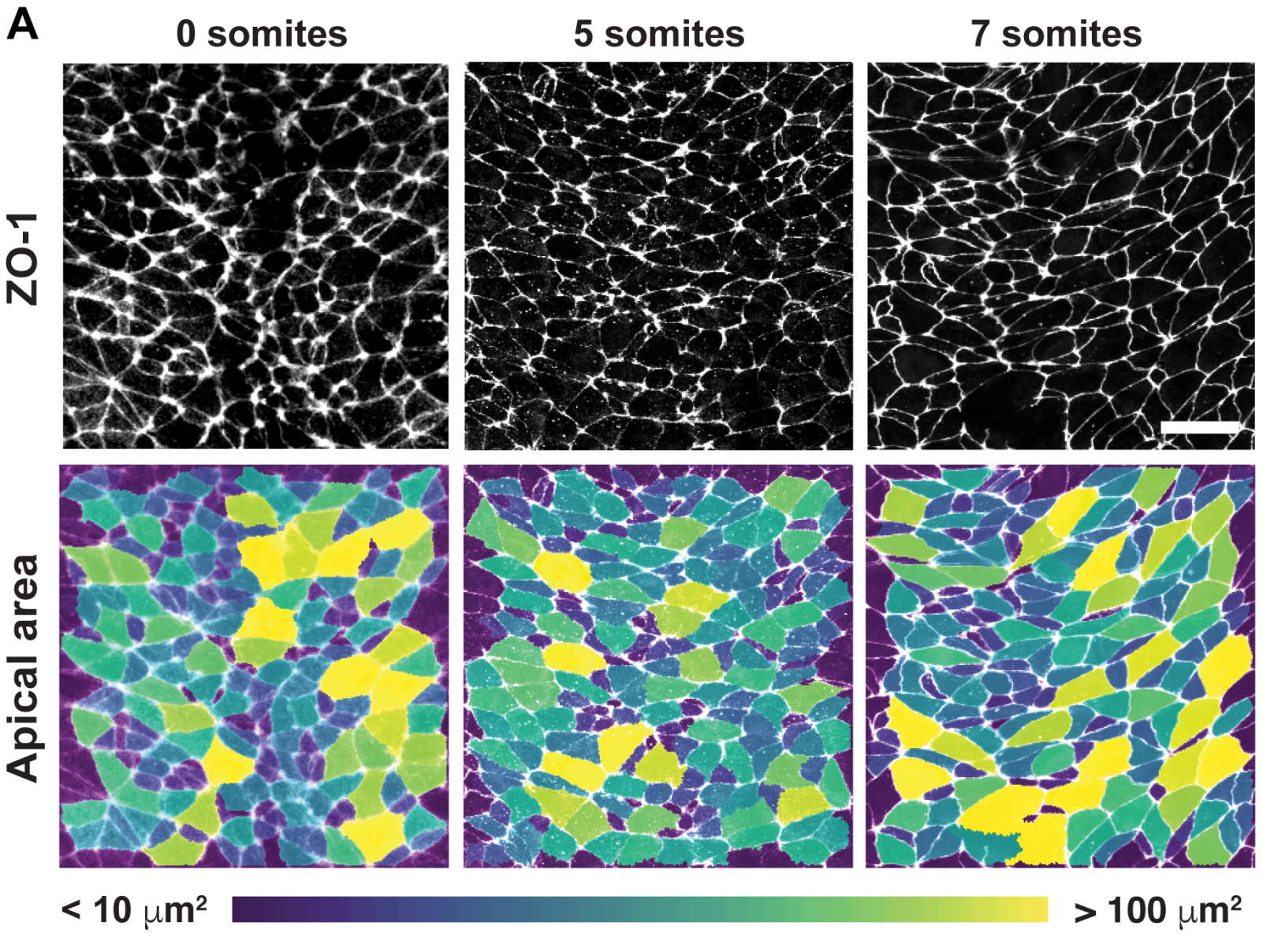

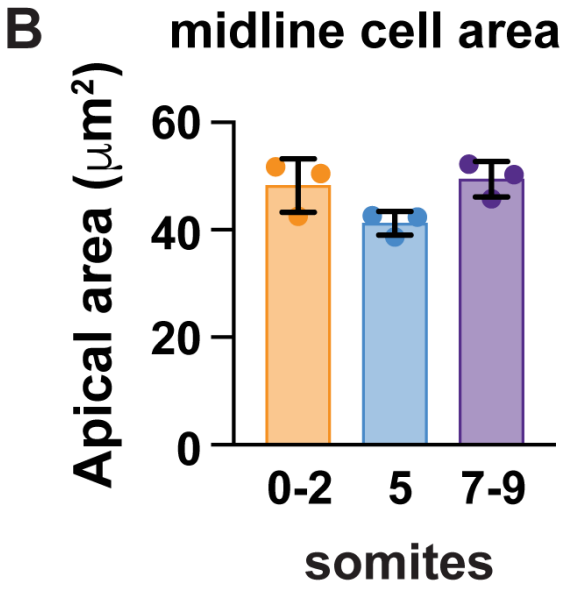

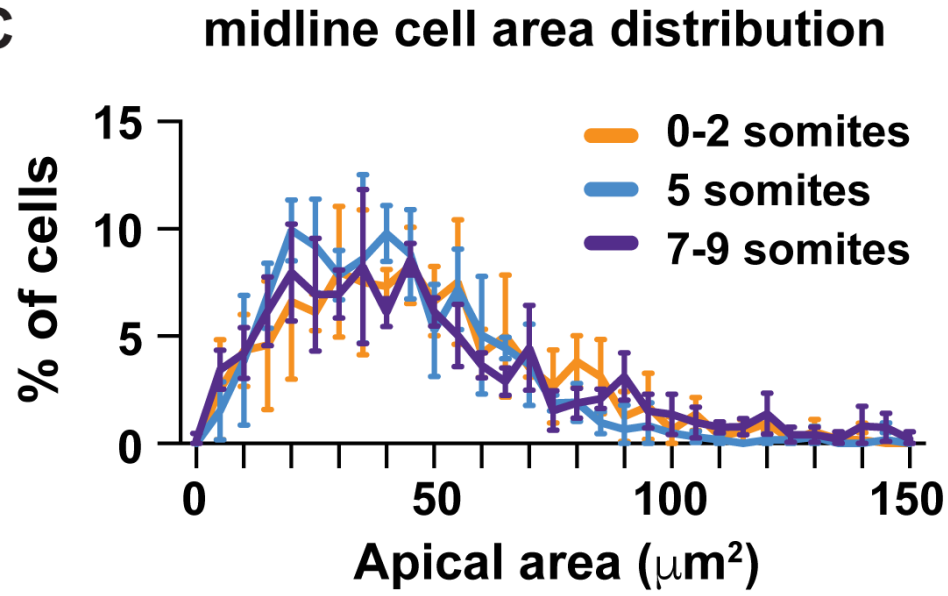

Figure 3

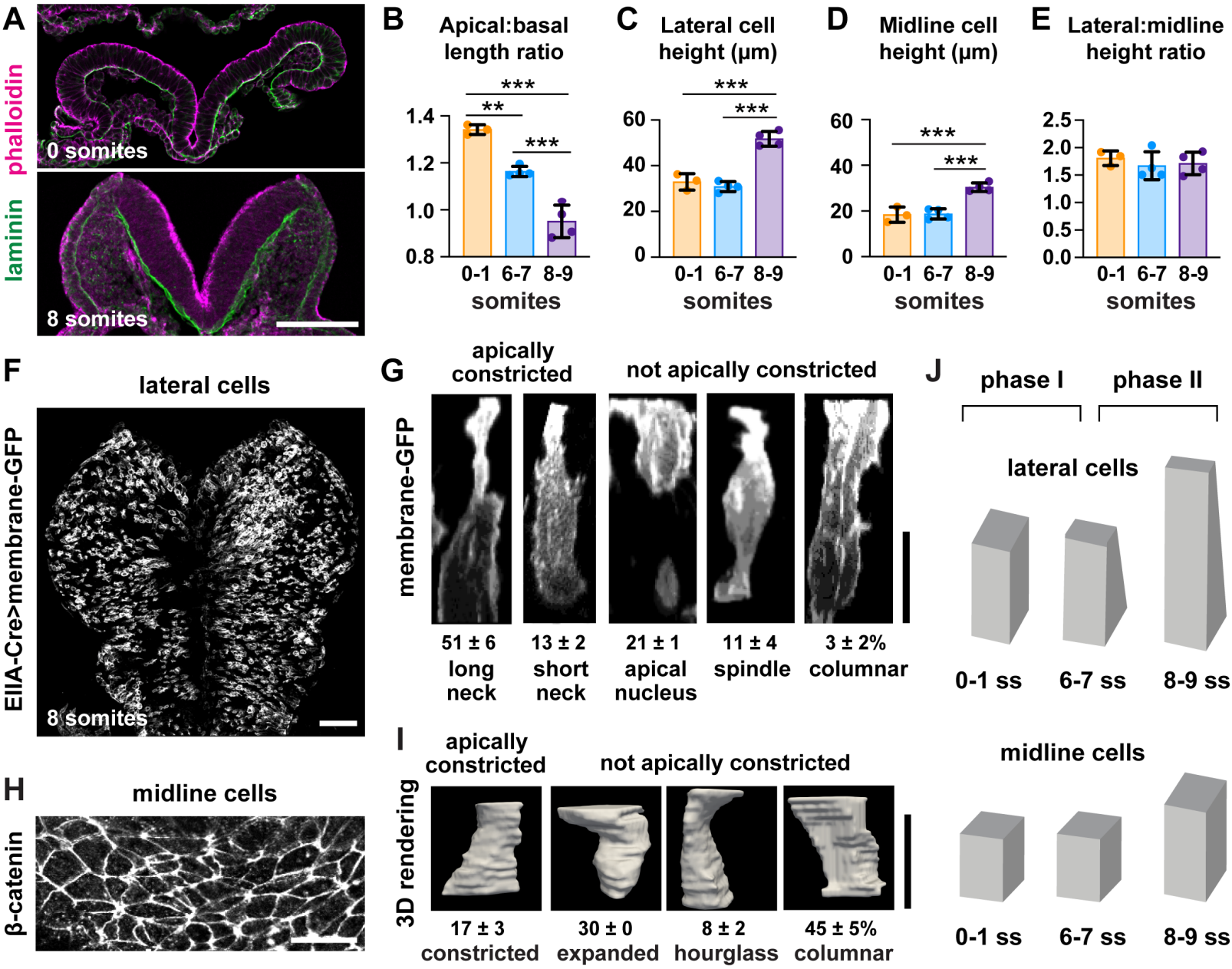

Figure 4

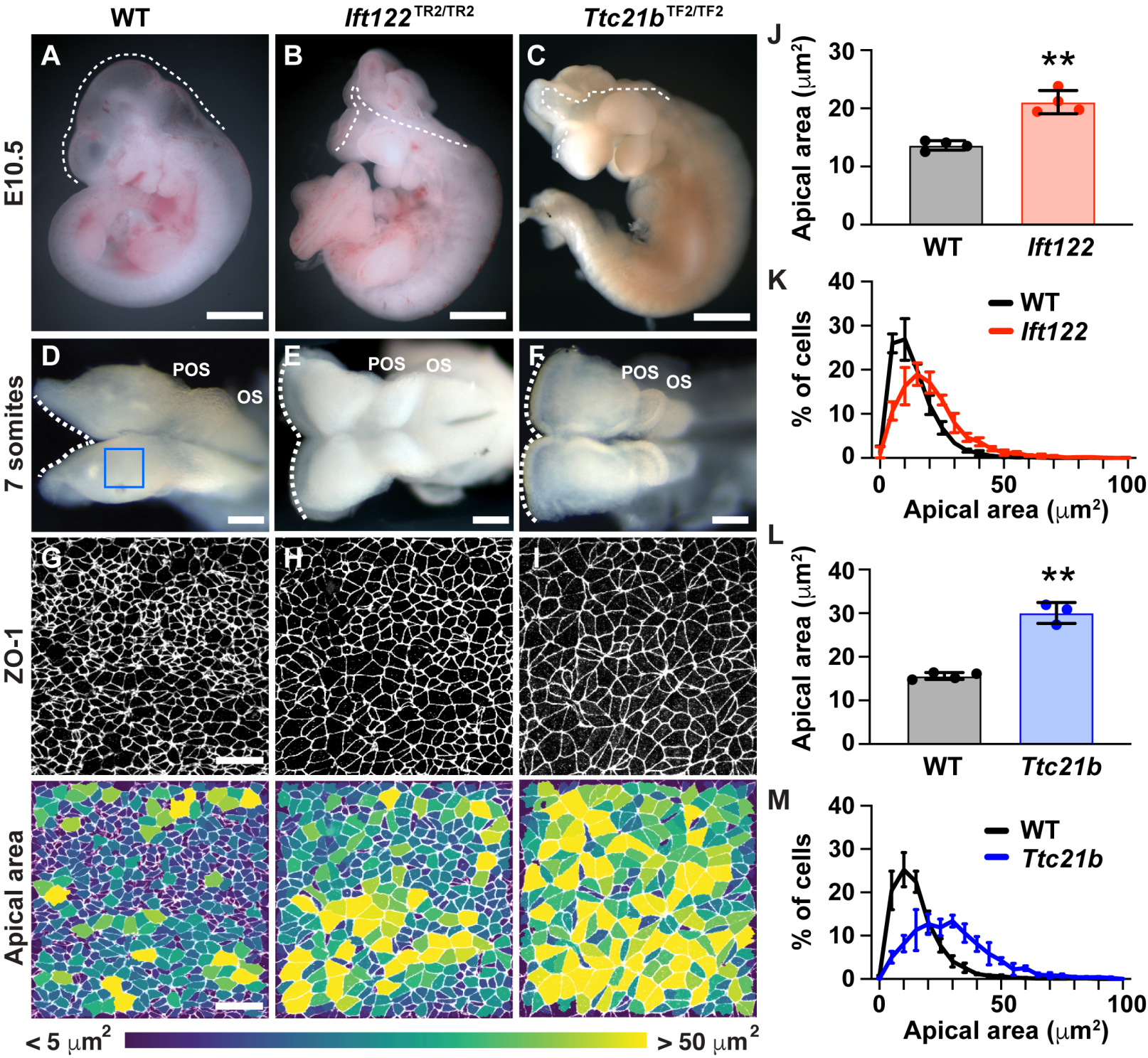

Figure 5

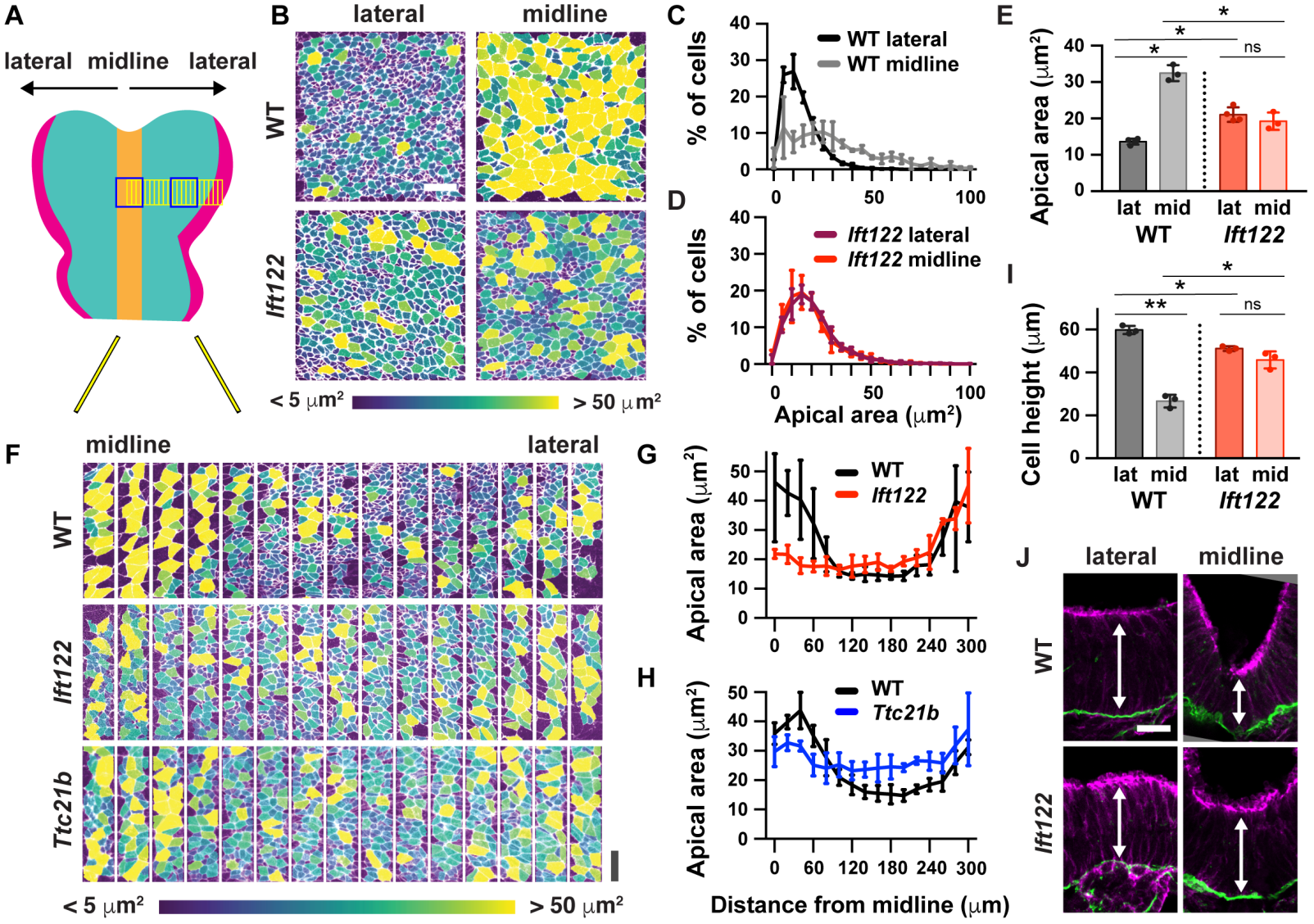

Figure 6

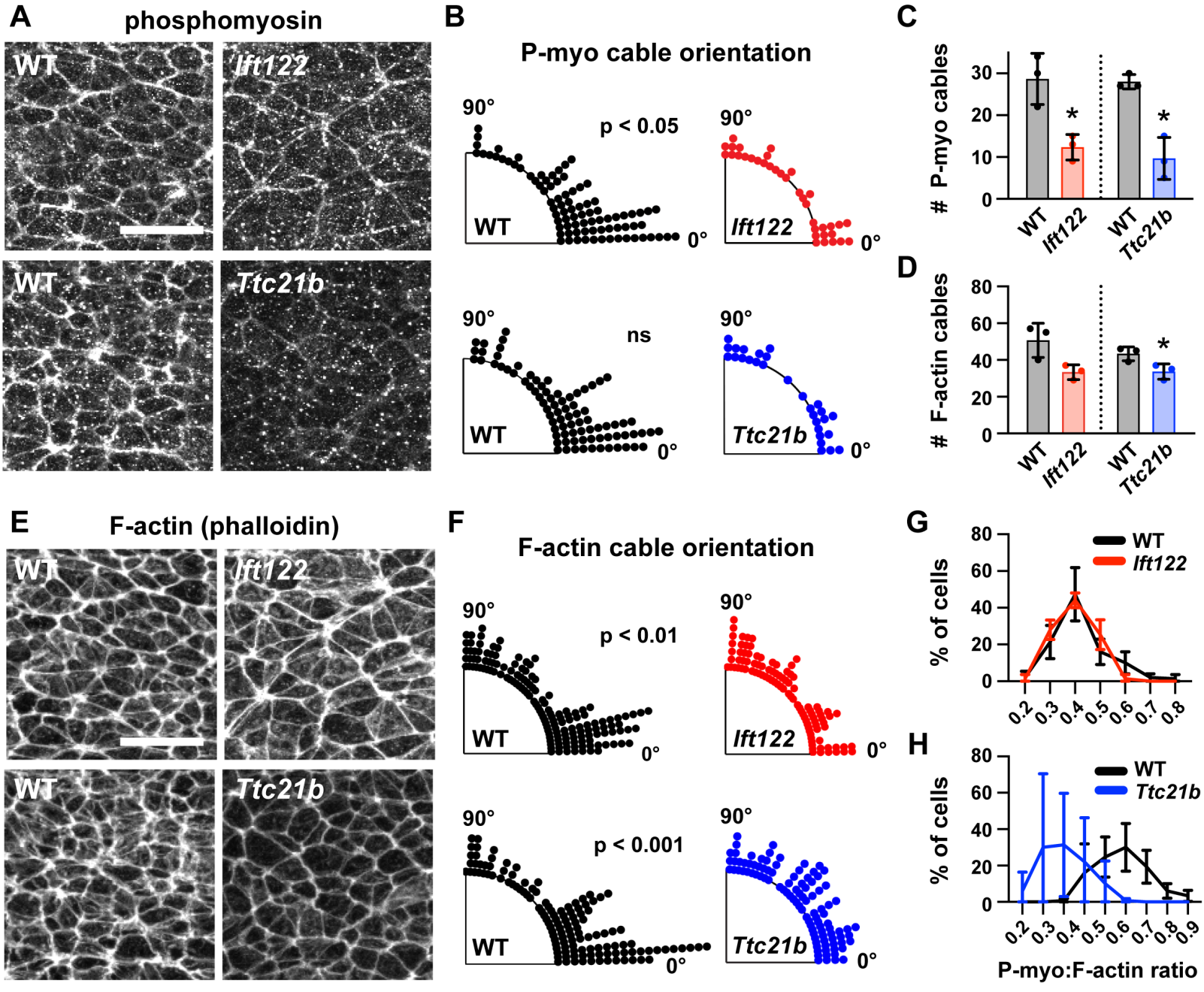

Figure 7

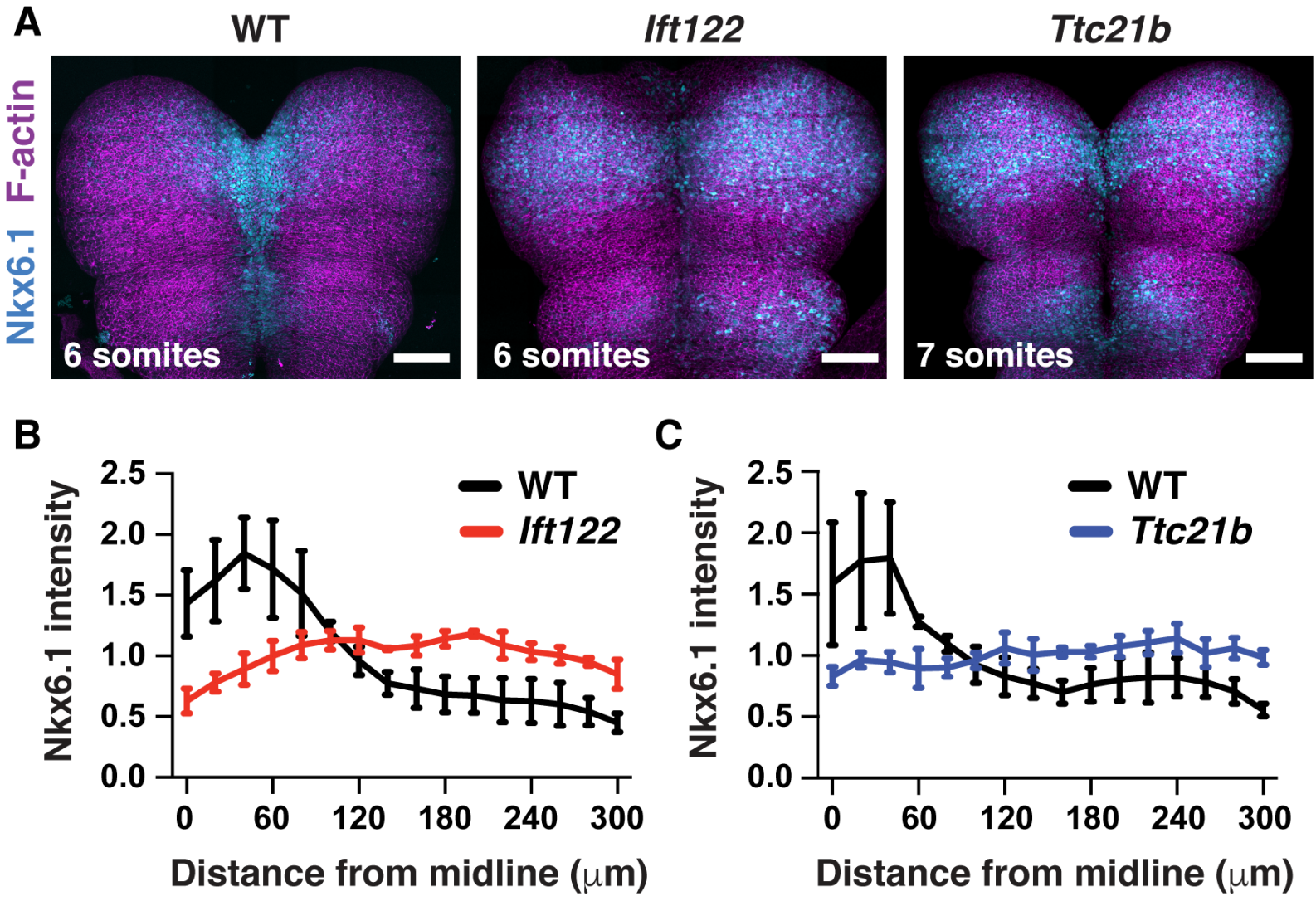

Figure 8

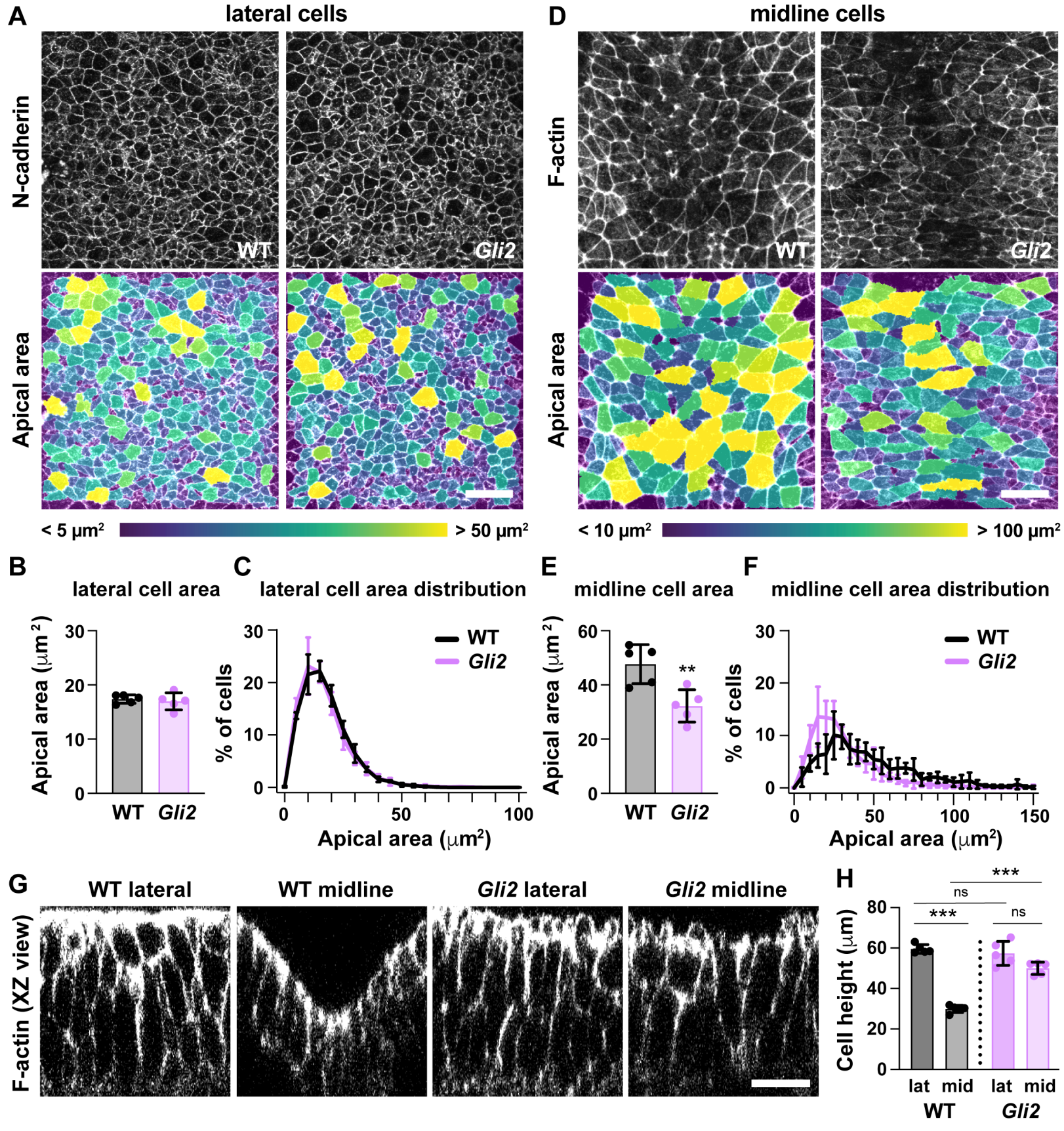

Figure 9